An Optimized Approach to Membrane Capacitance Estimation Using Dual-Frequency Excitation

David W. Barnett*§ and Stanley Misler*
*Departments of Medicine (Renal Division) and Cell Biology/Physiology, Washington University Medical Center, St. Louis, Missouri 63110, and §Department of Electrical Engineering, Saint Louis University, Parks College, Cahokia, Illinois 62206 USA

ABSTRACT We present an optimized solution to the problem of membrane impedance estimation when a patch-clamped cell is stimulated by a dual-frequency, sinusoidal excitation. The complete data set of raw whole-cell current samples is typically reduced, via digital lock-in detection, to measurements of the complex cell model admittance at the two stimulus frequencies. We describe a statistical model of both data sets and demonstrate that the admittance data adequately represent the essential features obtained from the raw data. The parameter estimates obtained by a nonlinear weighted least-squares solution (NWLS), which under normal recording conditions is equivalent to the maximum likelihood solution, essentially obtain the theoretical lower bound on variance established by the Cramér-Rao bound. Our software implementation of the NWLS solution produces estimates of the cell model parameters that are less noisy than other dual-frequency systems. Our system can be used 1) to measure slow changes in membrane capacitance in the face of large, slow changes in membrane resistance, 2) to detect with confidence capacitance changes expected from the exocytosis of moderate-sized dense core granules, and 3) to reduce the cross-talk between transient changes in membrane conductance and membrane capacitance.

INTRODUCTION

Over the past decade, measurements of membrane impedance have been widely used to estimate the changes in membrane capacitance associated with exocytosis of secretory granules in patch-clamped secretory cells. The secretory process can be initiated by depolarization (Neher and Marty, 1982; Gillis and Misler, 1992), introduction into the cytoplasm of second messengers (e.g., Ca^{2+} or $GTP_\gamma S$) via dialysis (Penner and Neher, 1988, 1989; Augustine and Neher, 1992; Barnett and Misler, 1995a) or flash photolysis of a caged compound (Heidelberger et al., 1994; Heinemann et al., 1994), or application of chemical secretogogues (Lindau and Fernandez, 1986; Fernandez et al., 1987). The impedance approach assumes that 1) a patch-clamped cell may be adequately modeled electrically as a three-element circuit, namely, an access resistance (R_a), from the recording pipette to the cell cytoplasm, in series with a parallel combination of the membrane resistance (R_m) and membrane capacitance (C_m), and 2) over the time course when C_m is assessed, R_a and R_m remain relatively constant.

Currently, the most widely used techniques for monitoring membrane impedance are digital-based and involve phase detection of a single-frequency sinusoidal wave with a lock-in amplifier. In one method (Lindau and Neher, 1988), often called the Lindau-Neher method (LN), the phase detector decomposes the phase-shifted current flowing in response to a sinusoidal excitation into real (in-phase) and imaginary (quadrature) components, which when scaled by the magnitude of the stimulus are equal to the parameters $A(\omega)$ and $B(\omega)$ of the admittance function, $Y(\omega)$, evaluated at the stimulus frequency ω. That is,

$$\begin{aligned} Y(\omega) &= A(\omega) + jB(\omega) \\ &= \frac{1 + \omega^2 R_m R_p C_m^2}{R_T(1 + \omega^2 R_p^2 C_m^2)} + j\frac{\omega R_m^2 C_m}{R_T^2(1 + \omega^2 R_p^2 C_m^2)}, \end{aligned} \quad (1)$$

where $R_T = R_a + R_m$ and $R_p = R_a \times R_m/R_T$. The DC component of the current, arising from the difference between the imposed holding potential (V_{DC}) and the reversal potential (E_{rev}) of the cell, provides the necessary third equation to solve for the values of the circuit parameters.

$$I_{DC} = \frac{V_{DC} - E_{rev}}{R_T}. \quad (2)$$

This method requires that E_{rev} remain constant or that it be easily tracked. In the second method, based on early experiments by Neher and Marty (1982), a piecewise-linear (PL) technique is used. This approach capitalizes on the fact that small changes in C_m result in a shift in the sinusoidal current that is roughly orthogonal to changes in the sinusoidal current that are induced by variations in both resistive elements. This approximation requires that R_m be much greater than $1/(\omega C_m)$ for the orthogonality to be valid. However, even under these circumstances, the task of finding and tracking the correct phase setting of the lock-in amplifier can be challenging and/or tedious, depending on the approach selected (Neher and Marty, 1982; Fidler and Fernandez, 1989; Joshi and Fernandez, 1988; Zierler, 1992), as well as error-prone (see the review by Gillis, 1995).

Received for publication 4 April 1996 and in final form 14 January 1997.
Address reprint requests to Dr. David W. Barnett, Renal Division, Yalem 815, Barnes-Jewish Hospital, North Campus, 216 S. Kingshighway, St. Louis, MO 63110. Tel.: 314-454-7719; Fax: 314-454-5136; E-mail: barnetdw@pxa.slu.edu.

0006-3495/97/04/1641/18 $2.00

At least two groups have recently developed techniques for dual-frequency sinusoidal excitation to estimate C_m under conditions where 1) R_m, and hence E_{rev}, changes simultaneously with C_m, e.g., with application of secretogogues that cause a rise in cytosolic Ca^{2+} (Rohlícek and Schmid, 1994), or 2) when R_m is very low (Donnelly, 1993). The use of two sinusoids at different frequencies provides for four equations (a pair at each frequency) and thus represents an overdetermined system in terms of the three unknowns (C_m, R_m, and R_a). However, both of the previously published algorithms present unoptimized, ad hoc algebraic solutions to the overdetermined problem.

In the first section of this paper we present a robust, engineering-based, nonlinear weighted least-squares (NWLS) approach for estimating the circuit parameters of a cell stimulated by a dual-frequency excitation. First, we characterize the "raw data," namely the many samples obtained over a fundamental period of the current waveform, by a statistical model in which both the mean and the covariance are functions of the unknown parameters. The raw data would provide the best parameter estimates, in terms of minimum variance, if the storage and computational costs were not prohibitive. (Here "best" refers to the theoretical lower bound on the variance of any unbiased parameter estimate, as established by the "Cramér-Rao Bound" (CRB) commonly associated with maximum likelihood (ML) estimation techniques.) We define the minimum bound using the raw data set and, subsequently, compare the effect of data reduction, as well as the performance of various algorithms to the theoretical limit. Second, we show that decreasing the size of the data set, via digital lock-in detection of the real and imaginary parts of the cell model admittance at the two stimulus frequencies, results in only a marginal increase in the CRB. Third, we demonstrate that a NWLS approach, based on the reduced data set, produces parameter estimates that essentially reach the CRB. For our reduced data set, the NWLS solution, using weighting factors that are determined from the statistical description of the reduced data, is equivalent to the ML solution.

In the second section of this paper we outline our software implementation of the NWLS solution and demonstrate that this results in estimates of the cell model parameters that are less noisy than those produced by other dual-frequency systems. This approach offers several promising features for capacitance measurement in neuroendocrine cells. First, although often noisier than single-frequency methods, the NWLS algorithm is still capable of reliably detecting the capacitance changes expected from the exocytosis of large dense core granules from chromaffin cells (~200–300 nm diameter). Second, using the NWLS approach we can limit cross-over of transient changes in membrane conductance into membrane capacitance estimates and hence limit artifactual transients in C_m estimates that mimic a rapid endocytotic process. These C_m transients can be especially prominent in cells displaying prolonged tail currents after excitation with depolarizing pulses. Last, in a companion study (Barnett et al., 1996) employing the NWLS method to examine exocytosis induced by the channel-forming neurotoxin, α-latrotoxin, we demonstrated that this optimized approach can be used to reliably detect slow changes in membrane capacitance in the face of simultaneous, progressive (up to 10-fold) changes in membrane resistance. Portions of this work have previously been presented in abstract form (Barnett and Misler, 1995b).

ELECTROPHYSIOLOGICAL METHODS

Rat adrenal medullary chromaffin cells were maintained as primary cultures on glass coverslips at 37°C in a HEPES/HCO_3- buffered Dulbecco's minimum essential medium enriched with fetal bovine serum, penicillin and streptomycin, and ascorbic acid (Neely and Lingle, 1992). Recordings were made at room temperature (20–23°C) in an extracellular solution (ES) of physiological Ringer's containing (in mM) 144 NaCl, 5.5 KCl, 2 $CaCl_2$, 1 $MgCl_2$, and 20 HEPES titrated to pH 7.35 with NaOH. Some experiments used a modified ES that replaced 50 mM NaCl with the equivalent concentration of tetraethylammonium chloride (TEA_{50}-ES). Voltage-clamp recordings were made according to our laboratory's protocol for the perforated patch variant of a whole-cell recording (Barnett et al., 1995) using an EPC-9 patch-clamp amplifier (HEKA elektronik Gmbh, Lambrecht, Germany). The tips of the patch pipettes were filled with either a standard high K^+ (K^+-IS) or high Cs^+ (Cs^+-IS) internal solution. The K^+-IS consisted of (in mM) 65 KCl, 28.4 K_2SO_4, 11.3 NaCl, 1 $MgCl_2$, 0.5 EGTA, 47.2 sucrose, and 20 HEPES titrated to pH 7.3 with potassium hydroxide (KOH). In the case of Cs^+-IS, the KCl and K_2SO_4 were substituted, mole for mole, with CsCl and Cs_2SO_4, respectively. The pipettes were then back-filled with the selected internal solution, containing an additional 250 μg/ml of nystatin. The membrane potential was held at a DC value of −70 mV, except for brief intervals when voltage-dependent currents were evoked in response to brief depolarizing pulses. The algorithm for estimating the membrane parameters involves a digitally generated, dual-frequency stimulus that is the topic of the remainder of the paper. Amperometric measurements of catecholamine secretion were made as previously described (Zhou and Misler, 1996), using polypropylene insulated micro-carbon fiber electrodes (8–10 μm diameter), the tips of which were micropositioned on the surface of the chromaffin cells and held at +780 mV by an EPC-7 patch-clamp amplifier (HEKA elektronik Gmbh).

RESULTS

Part I: analysis of the membrane impedance parameter estimation problem

Description of the "raw" current samples

The development of this method is based on the commonly accepted three-parameter circuit model of a spherical cell

described previously. The admittance transfer function of the cell (note $s = j\omega$) is typically expressed in terms of C_m, R_m, and R_a (recall Eq. 1), as defined by the left-hand expression of Eq. 3. However, because this is a nonlinear function of all three parameters, it is more convenient to work with the standard transfer function coefficients, as shown in the right-hand expression of Eq. 3, which contains only one nonlinear term (a_1):

$$Y(s) = \frac{1 + sC_mR_m}{R_T(1 + sC_mR_p)}, \quad \text{or} \quad Y(s) = \frac{b_0 + sb_1}{1 + sa_1}. \tag{3}$$

Because there is an invertible transformation between these two sets of parameters, solving for the transfer function coefficients is equivalent to finding the circuit model parameters:

$$R_a = \frac{a_1}{b_1}, \quad R_m = \frac{b_1 - a_1b_0}{b_0b_1}, \quad C_m = \frac{b_1^2}{b_1 - a_1b_0}. \tag{4}$$

Assuming that a sinusoidal voltage waveform is applied to the cell, measurements of the real and imaginary parts of the admittance, at the stimulus frequency, can be obtained from an analog or digital lock-in amplifier with an effective phase setting of 0°, i.e., having accounted for the phase shift due to various system components.

$$Y(\omega) = \frac{b_0 + \omega^2a_1b_1}{1 + \omega^2a_1^2} + j\frac{\omega(b_1 - a_1b_0)}{1 + \omega^2a_1^2} = A(\omega) + jB(\omega). \tag{5}$$

In the case of a dual-frequency voltage stimulus applied to the previous cell admittance, the stimulus and corresponding resultant current are given by

$$\begin{aligned} v(t) &= V_1\cos(\omega_1 t) + V_2\cos(\omega_2 t), \\ i(t) &= V_1(A_1\cos(\omega_1 t) - B_1\sin(\omega_1 t)) \\ &\quad + V_2(A_2\cos(\omega_2 t) - B_2\sin(\omega_2 t)), \end{aligned} \tag{6}$$

(note that $A_1 = A(\omega_1)$, etc.). At the input of the patch-clamp amplifier, the actual measured signal $x(t)$ includes an additional Gaussian noise term, as diagrammed in Fig. 1, that will be described in a later section.

The stimulus will be restricted such that the applied frequencies are integer multiples of some base frequency, i.e., $\omega_1 = k_1\omega_0$ and $\omega_2 = k_2\omega_0$, where typically $k_1 = 1$ and $k_2 = 2$ or 3. This requirement ensures that, for a parameter estimation rate equal to the base frequency, there are an integer number of complete sinusoidal periods for the two distinct signals. The computer then samples N points over one period of the base frequency, i.e., the sample period (T) is $T = (2\pi)/(N\omega_0)$, resulting in an N-dimensional random vector $\mathbf{x}$ consisting of the $N \times 1$ column vector $\mathbf{i}$ of "raw" current samples and the noise vector $\mathbf{n}$, which is also $N \times 1$:

$$\mathbf{x} = \mathbf{i} + \mathbf{n}, \quad \mathbf{x} = \begin{bmatrix} x(0) \\ \vdots \\ x(N-1) \end{bmatrix}, \quad \mathbf{n} = \begin{bmatrix} n(0) \\ \vdots \\ n(N-1) \end{bmatrix}. \tag{7}$$

However, the current samples can also be expressed in terms of the $N \times 4$ mode matrix $\mathbf{D}$, which contains samples of the cosine and sine vectors at each stimulus frequency (the column vectors $\mathbf{C}_f$ and $\mathbf{S}_f$, where the subscript f indicates the frequency ω_1 or ω_2) and the mode weights θ_{AB}. Here the sample vector becomes

$$\mathbf{x} = \mathbf{D}\theta_{AB} + \mathbf{n}, \quad \mathbf{D} = [\mathbf{C}_1 \mid -\mathbf{S}_1 \mid \mathbf{C}_2 \mid -\mathbf{S}_2],$$
$$\theta_{AB} = \begin{bmatrix} A_1 \\ B_1 \\ A_2 \\ B_2 \end{bmatrix}, \tag{8}$$

where

$$\mathbf{C}_f = V_f\begin{bmatrix} 1 \\ \cos\left(\frac{2\pi k_f}{N}\right) \\ \vdots \\ \cos\left(\frac{2\pi k_f}{N}(N-1)\right) \end{bmatrix}, \quad \mathbf{S}_f = V_f\begin{bmatrix} 0 \\ \sin\left(\frac{2\pi k_f}{N}\right) \\ \vdots \\ \sin\left(\frac{2\pi k_f}{N}(N-1)\right) \end{bmatrix}.$$

The mode weights, representing the real and imaginary parts of the admittance, can be written in terms of the nonlinear portion of the transfer function, i.e., the 4×2 matrix $\mathbf{H}$, which is strictly a function of the a_1 parameter, and the linear parameters b_0 and b_1, which are combined to make the 2×1 vector $\mathbf{b}$. It will be convenient at times to refer to both the transfer function parameters and the circuit model parameters in vector notation, given as θ and $\mathbf{w}$, respectively. These terms are summarized as follows:

$$\mathbf{x} = \mathbf{DHb} + \mathbf{n},$$
$$\mathbf{H} = \mathbf{H}(a_1) = \begin{bmatrix} \frac{1}{1 + \omega_1^2a_1^2} & \frac{\omega_1^2a_1}{1 + \omega_1^2a_1^2} \\ \frac{-\omega_1a_1}{1 + \omega_1^2a_1^2} & \frac{\omega_1}{1 + \omega_1^2a_1^2} \\ \frac{1}{1 + \omega_2^2a_1^2} & \frac{\omega_2^2a_1}{1 + \omega_2^2a_1^2} \\ \frac{-\omega_2a_1}{1 + \omega_2^2a_1^2} & \frac{\omega_2}{1 + \omega_2^2a_1^2} \end{bmatrix}, \quad \mathbf{b} = \begin{bmatrix} b_0 \\ b_1 \end{bmatrix}, \tag{9}$$
$$\mathbf{Hb} = \theta_{AB}, \quad \theta = \begin{bmatrix} b_0 \\ b_1 \\ a_1 \end{bmatrix}, \quad \text{and} \quad \mathbf{w} = \begin{bmatrix} R_a \\ R_m \\ C_m \end{bmatrix}.$$

Although the focus is on a dual-frequency stimulus, the method can easily be extended to include additional stimuli by appropriate modification of the $\mathbf{D}$ matrix (two additional columns per frequency) and the $\mathbf{H}$ matrix (two additional rows per frequency).

In standard whole-cell or perforated-patch recording, the output noise is primarily due to the thermal noise that exists in the resistive elements (R_a and R_m) of the cell rather than amplifier noise, as in the case of single-channel recording

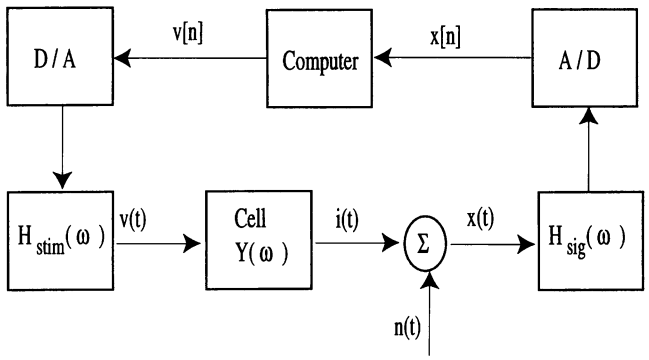

FIGURE 1 Signal-processing block diagram tracing the path from the computer-generated voltage stimulus through the D/A converter and the patch-clamp pre-filters (H_{stim}) to the cell model $Y(\omega)$. The current measured by the amplifier ($i(t)$) is corrupted by a noise signal ($n(t)$), the spectral properties of which are a function of the cell parameters. This signal is subsequently filtered (H_{sig}) before being sampled by the A/D and recorded by the computer.

(Hamill et al., 1981). These resistances can be modeled as ideal elements in series with a Gaussian, zero-mean, white-noise voltage source defined by the flat spectrum $S_V = 2kTR$ (or, equivalently, in parallel with a current source characterized by $S_I = 2kT/R$), where the individual terms are the Boltzmann constant k, the absolute temperature T, and value of the resistance R (Papoulis, 1991). The spectrum of the current noise that is measured at the input of the patch-clamp amplifier is ultimately shaped by the admittance of the cell. Superposition of the two noise sources, due to R_a and R_m, yields the following result:

$$S_I(\omega) = 2kT\frac{b_0 + \omega^2 a_1 b_1}{1 + \omega^2 a_1^2} = 2kT\,\mathrm{Re}\{Y(\omega)\}, \qquad (10)$$

which is clearly a function of the parameter vector θ. In a typical cell (i.e., $R_m > R_a$), the current noise spectral density is smaller at low frequencies, because of the large value of R_m, and increases with frequency to a plateau level proportional to $1/R_a$, similar to the general shape of the admittance. However, this broad-band noise spectrum is eventually low-pass filtered by the patch-clamp amplifier before sampling by the A/D. The resulting spectrum is defined as

$$S(\omega) = S_I(\omega)|H_{sig}(\omega)|^2, \qquad (11)$$

where H_{sig} represents the system transfer function, presumably known, of the combined filter stages found in the amplifier signal pathway (recall Fig. 1).

To determine the density function on the random vector $\mathbf{x}$, the structure of the $N \times N$ noise covariance matrix, i.e., $\mathbf{R} = E[\mathbf{n}\mathbf{n}^T]$, must first be ascertained. Having defined the noise spectral density, the continuous-time autocorrelation function can be determined via the Fourier transform relationship:

$$r_a(\tau) = \frac{1}{2\pi}\int_{-\infty}^{\infty} S(\omega)e^{i\omega\tau}\,d\omega, \qquad (12)$$

which leads directly to the covariance function because the noise is zero-mean. The transform is dependent on the patch-clamp amplifier due to the effect of the signal filters; however, regardless of the particular amplifier, the solution will always be a function of the known amplifier characteristics and the unknown cell parameters (see Barnett, 1995, for a solution of this transform for the EPC-9 amplifier). Finally, taking into account the even nature of correlation functions, the noise covariance matrix can be expressed as samples (index $m = 0 \ldots N - 1$, T = sample period) of the continuous time autocorrelation function, $r(m) = r_a(mT)$, resulting in the Toeplitz matrix R, the elements of which are given by $R_{ij} = r(j - i)$. A simulated autocorrelation function and noise spectrum are shown in Fig. 2 for typical cell parameters.

Having defined the mean and covariance, the density function for the vector $\mathbf{x}$ may now be specified. In general, the random sample may contain M independent, identically distributed (i.i.d.) random vectors (we assume that the M sample vectors are drawn from a wide-sense stationary process). The number of sample vectors used per estimate (M) is in essence the filter factor on the parameter estimates; e.g., for a base frequency of 400 Hz, single-sample vectors are generated every 2.5 ms, so that $M = 40$ roughly corresponds to a 100-ms time-constant filter. Therefore we may

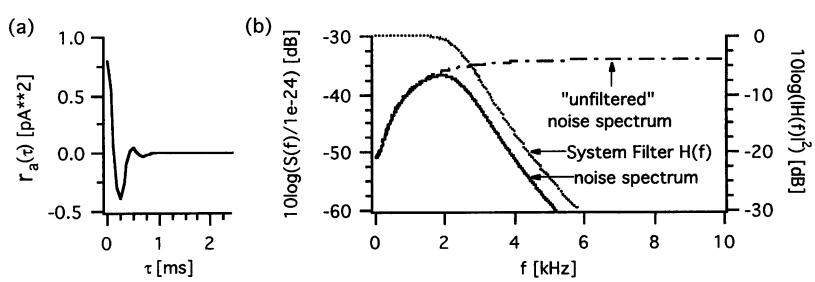

FIGURE 2 (*a*) Autocorrelation function of the sampled current based on a simulated cell model (R_a = 20 MΩ, R_m = 1000 MΩ, and C_m = 5 pF) and the theoretical characteristics of an EPC-9 amplifier (signal filters set to FILT1 = 10 kHz Bessel and FILT2 = 2.5 kHz Butterworth). (*b*) The "filtered" and the "unfiltered" version of the noise spectrum, associated with the autocorrelation function illustrated in *a*, are plotted using the left axis. The overall frequency response of the EPC-9 amplifier system is referenced to the right axis.

write the multivariate normal density function for M i.i.d., N-dimensional sample vectors of $\mathbf{x}$ as

$$f_\theta(\mathbf{x}_1, \ldots, \mathbf{x}_M) = (2\pi)^{-MN/2}|\mathbf{R}|^{-M/2}e^{-1/2\sum_{i=1}^{M}(\mathbf{x}_i-\mathbf{DHb})^T\mathbf{R}^{-1}(\mathbf{x}_i-\mathbf{DHb})}, \quad (13)$$

where both the mean (**DHb**) and the covariance (**R**) are functions of the transfer function coefficients.

Description of the "reduced" admittance data

Although the raw data (i.e., **N** samples per base period) are available if the system is software based, it is often impracticable to save every sample, because of memory limitations. Therefore, the actual data that are saved and subsequently available for analysis are the measurements of the real and imaginary parts of the admittance obtained from the outputs of a dual-frequency digital lock-in amplifier. This data reduction typically decreases the storage requirements by 50–80%.

The dual-frequency digital lock-in amplifier is essentially a discrete Fourier transform (DFT), evaluated at the frequencies ω_1 and ω_2, of the windowed process $x[n]$, which is represented by the vector $\mathbf{x}$ (one period of samples). This linear transformation of the raw data vector $\mathbf{x}$ to the reduced data $\mathbf{y}$ is given by the equation

$$\mathbf{y} = (\mathbf{D}^T\mathbf{D})^{-1}\mathbf{D}^T\mathbf{x}, \quad (14)$$

where the mode matrix $\mathbf{D}$ was defined previously and the first term reduces to a diagonal scaling matrix:

$$(\mathbf{D}^T\mathbf{D})^{-1} = \mathrm{diag}\left\{\frac{2}{V_1^2N} \quad \frac{2}{V_1^2N} \quad \frac{2}{V_2^2N} \quad \frac{2}{V_2^2N}\right\}. \quad (15)$$

Because this is a linear transformation, the mean vector and covariance matrix for $\mathbf{y}$ are simply given as

$$\mathbf{m}_y = \mathbf{Hb} \text{ and } \mathbf{R}_y = (\mathbf{D}^T\mathbf{D})^{-1}\mathbf{D}^T\mathbf{R}\mathbf{D}(\mathbf{D}^T\mathbf{D})^{-1}, \quad (16)$$

which results in the new density function for the $\mathbf{y}$ data:

$$f_\theta(\mathbf{y}) = (2\pi)^{-MN/2}|\mathbf{R}_y|^{-M/2}e^{-1/2\sum_{i=1}^{M}(\mathbf{y}_i-\mathbf{Hb})^T\mathbf{R}_y^{-1}(\mathbf{y}_i-\mathbf{Hb})}, \quad (17)$$

The diagonal elements of $\mathbf{R}_y$ are approximately the DFT of the windowed covariance function and thus correspond to a smoothed version of the noise power spectrum evaluated at the stimulus frequencies. These elements, as well as the nontrivial off-diagonal elements, are detailed in Appendix A. Although the off-diagonal elements are generally substantial (within 1–2 orders of magnitude of the diagonal elements), there are two general cases that produce an $\mathbf{R}_y$ matrix that is dominated by the diagonal terms. The first case occurs when the original correlation function becomes narrow, i.e., when the noise spectrum becomes wide-band. The second case results when the length of the sample vector is increased while the sample period is maintained constant. In the limit of the second example, consider the situation in which samples of $x[n]$ are obtained over all time (i.e., no window), where $\mathbf{R}_y$ would reduce to the diagonal matrix:

$$\mathbf{R}_y = \mathrm{diag}\left\{\frac{\pi S(\omega_1)}{V_1^2} \quad \frac{\pi S(\omega_1)}{V_1^2} \quad \frac{\pi S(\omega_2)}{V_2^2} \quad \frac{\pi S(\omega_2)}{V_2^2}\right\}, \quad (18)$$

where the variance of the $\mathbf{y}$ elements is simply proportional to the inverse of the signal-to-noise ratio (SNR) at the particular frequencies.

Because our parameter estimates will be based on the reduced data set, we examined the overall impact of the transformation by determining whether $\mathbf{y}$ provides the same information about θ as the full data set. Unfortunately, since the covariance matrix depends on θ, $\mathbf{y}$ is not a sufficient statistic for θ (Barnett, 1995). Qualitatively, because the noise spectrum is shaped by the cell parameters, by observing only the noise (no signal) we could arrive at an estimate of the model circuit, albeit a noisy estimate. (Conceptually, this is similar to the wide-band stimulus approach of Clausen and Fernandez, 1981.) Thus by reducing the data set we are ignoring most of the noise-only information and focusing on the signal subspace, which is unaffected by the linear transformation and dominated by the information contained in the mean (due to the sinusoidal stimuli) rather than the information in the covariance matrix (due to the noise).

The Cramér-Rao Bound

The Cramér-Rao Bound (CRB) establishes a lower bound on the error covariance matrix of any unbiased estimator of the parameter vector θ (see Scharf, 1991, or van Trees, 1968, for a thorough review of ML estimators and the CRB). The CRB states that the error covariance of the estimator $\mathbf{C}$ is greater than or equal to the inverse of the Fisher Information matrix $\mathbf{J}$, which is the covariance of the "score," i.e., the derivative of the log-likelihood function. As a consequence of this, the mean square error for the θ_i parameter is greater than or equal to the corresponding diagonal element of the inverse of the Fisher Information matrix:

$$\mathbf{C} = E\{(\hat{\theta} - \theta)(\hat{\theta} - \theta)^T\} \geq \mathbf{J}^{-1}$$
$$\Rightarrow \mathbf{C}_{ii} = E\{(\hat{\theta}_i - \theta_i)^2\} \geq (\mathbf{J}^{-1})_{ii}. \quad (19)$$

Furthermore, given the $\mathbf{J}(\theta)$ matrix, the CRB for the cell model parameters can be derived from the corresponding Fisher Information matrix for the $\mathbf{w}$ vector as determined from the transformation $\mathbf{J}(\mathbf{w}) = \mathbf{G}\mathbf{J}(\theta)\mathbf{G}^T$, where the elements of the $\mathbf{G}$ matrix are $G_{ij} = \partial\theta_j/\partial w_i$ (Barnett, 1995).

For the reduced data set, the Fisher Information matrix $\mathbf{J}(\theta)$ can be written as the sum of two separate matrices (Ψ and Ξ), where the Ψ matrix represents the information found in the mean and the Ξ matrix corresponds to the

noise-only information:

$$\mathbf{J}(\theta) = \Psi(\theta) + \Xi(\theta),$$

$$\Psi(\theta) = M\begin{bmatrix} \mathbf{H}^T\mathbf{R}_y^{-1}\mathbf{H} & \mathbf{H}^T\mathbf{R}_y^{-1}\dfrac{\partial \mathbf{H}}{\partial a_1}\mathbf{b} \\ \mathbf{b}^T\dfrac{\partial \mathbf{H}^T}{\partial a_1}\mathbf{R}_y^{-1}\mathbf{H} & \mathbf{b}^T\dfrac{\partial \mathbf{H}^T}{\partial a_1}\mathbf{R}_y^{-1}\dfrac{\partial \mathbf{H}}{\partial a_1}\mathbf{b} \end{bmatrix}, \quad (20)$$

Calculation of Ψ requires the derivative of the $\mathbf{H}$ matrix with respect to the parameter a_1,

$$\frac{\partial \mathbf{H}}{\partial a_1} = \begin{bmatrix} \dfrac{-2\omega_1^2 a_1}{(1+\omega_1^2 a_1^2)^2} & \dfrac{\omega_1^2(1-\omega_1^2 a_1^2)}{(1+\omega_1^2 a_1^2)^2} \\ \dfrac{\omega_1(1-\omega_1^2 a_1^2)}{(1+\omega_1^2 a_1^2)^2} & \dfrac{-2\omega_1^3 a_1}{(1+\omega_1^2 a_1^2)^2} \\ \dfrac{-2\omega_2^2 a_1}{(1+\omega_2^2 a_1^2)^2} & \dfrac{\omega_2^2(1-\omega_2^2 a_1^2)}{(1+\omega_2^2 a_1^2)^2} \\ \dfrac{\omega_2(1-\omega_2^2 a_1^2)}{(1+\omega_2^2 a_1^2)^2} & \dfrac{-2\omega_2^3 a_1}{(1+\omega_2^2 a_1^2)^2} \end{bmatrix}, \quad (21)$$

whereas the individual elements of Ξ are determined using the matrix trace operation on a product containing both the inverse and the derivative of the covariance matrix $\mathbf{R}$ (for details, see Barnett, 1995):

$$\Xi(\theta)_{ij} = \frac{M}{2}\,\mathrm{tr}\left\{\mathbf{R}_y^{-1}\frac{\partial \mathbf{R}_y}{\partial \theta_i}\mathbf{R}_y^{-1}\frac{\partial \mathbf{R}_y}{\partial \theta_j}\right\}. \quad (22)$$

Because the Fisher Information matrix is proportional to the number of sample vectors M, the limit on the variance is simply inversely proportional to this factor.

In most cases, where the sinusoidal signals are large compared to the inherent cell noise, the elements of Ξ contribute little to the Fisher Information matrix. Fig. 3 illustrates that for a typical cell (C_m = 5 pF, R_a = 20 MΩ, and R_m = 1000 MΩ, f_1 = 400 Hz, f_2 = 800 Hz, M = 40) with equal magnitude stimuli, the inclusion of the Ξ matrix in the calculation of CRB was negligible (sub fF, MΩ, and kΩ for C_m, R_m, and R_a, respectively) for individual stimulus levels in the 1–10-mV range. Note that all calculations of the CRB were performed using the complete theoretical description of the covariance matrix (i.e., see Eq. 16 and Barnett, 1995).

Nonlinear weighted least squares

A complete maximum likelihood solution to the cell parameter estimation problem is quite computationally intensive, even when using the reduced data set (Barnett, 1995). However, if the covariance matrix is independent of θ, then the ML solution reduces to a weighted least-squares (WLS) problem with symmetrical weight matrix $\mathbf{Q} = \mathbf{R}_y^{-1}$ (Scharf, 1991). In our problem, the information contained in the covariance matrix is negligible compared to that of the mean, as measured by its insignificant contribution to the Fisher Information matrix; thus the WLS solution should approximate the ML solution. The WLS method minimizes the weighted squared error, i.e., the cost function C,

$$\min_{\theta} C(\theta) = \min_{\theta}\{(\mathbf{y} - \mathbf{Hb})^T\mathbf{Q}(\mathbf{y} - \mathbf{Hb})\}. \quad (23)$$

This is a nonlinear method (NWLS) because $\mathbf{H}$ is nonlinear in a_1. However, the nonlinearity is only a function of a scalar parameter, which is computationally simpler than working with a vector of nonlinear parameters, as would be necessary if the problem were left in terms of the circuit model elements instead of using the transfer function parameters. An iterative solution (Spanos and Mingor, 1993) can be formulated as follows. Given the kth estimate of a_1, the solution for $\mathbf{b}$ is simply the linear least-squares solution:

$$\mathbf{b}_k = (\mathbf{H}(a_{1_k})^T\mathbf{Q}\mathbf{H}(a_{1_k}))^{-1}\mathbf{H}(a_{1_k})^T\mathbf{Q}\mathbf{y}. \quad (24)$$

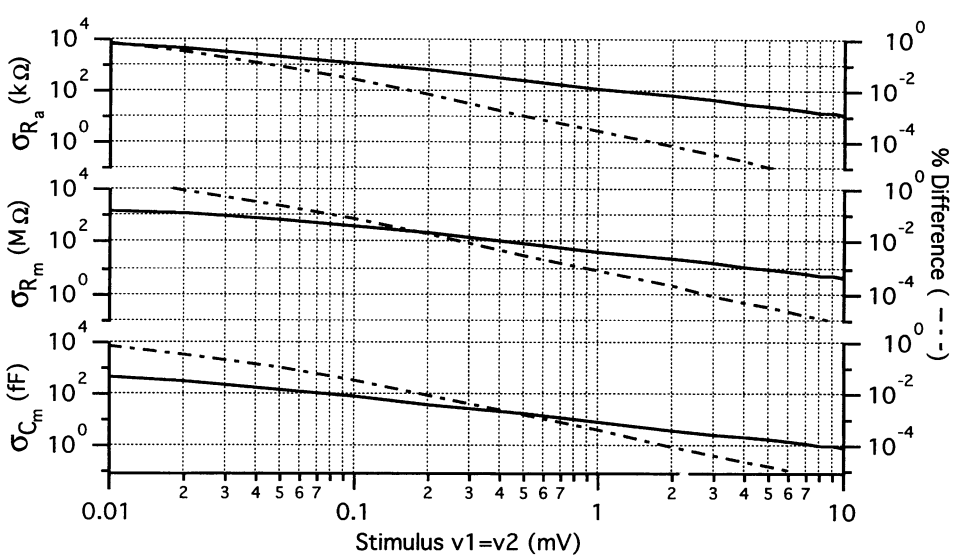

FIGURE 3 (*Left axis*) The minimum noise levels as determined from the CRB are shown as a function of stimulus level (v_1 = v_2) for a cell described by the base parameters: C_m = 5 pF, R_a = 20 MΩ, and R_m = 1000 MΩ. (*Right axis*) In the normal stimulus range (1–10 mV), the percentage difference between the true CRB and the CRB obtained by ignoring the noise-only contribution to the Fisher information matrix is negligible.

Forming the quadratic approximation to the cost function and inserting the estimate of $\mathbf{b}$ produces the following:

$$C(a_1) = (\mathbf{y} - \mathbf{H}(a_{1_k})\mathbf{b}_k)^T\mathbf{Q}(\mathbf{y} - \mathbf{H}(a_{1_k})\mathbf{b}_k) + (a_1 - a_{1_k})g_k + \frac{1}{2}(a_1 - a_{1_k})^2 G_k. \quad (25)$$

The first and second derivatives are defined as

$$g_k = -2\mathbf{b}^T \frac{\partial \mathbf{H}^T}{\partial a_1} \mathbf{Q}(\mathbf{y} - \mathbf{H}\mathbf{b}) \Big|_{a_{1_k}, b_k},$$

and

$$G_k = 2\mathbf{b}^T \frac{\partial \mathbf{H}^T}{\partial a_1} \mathbf{Q} \frac{\partial \mathbf{H}}{\partial a_1} \mathbf{b} - 2\mathbf{b}^T \frac{\partial^2 \mathbf{H}}{\partial a_1^2} \mathbf{Q}(\mathbf{y} - \mathbf{H}\mathbf{b}) \Big|_{a_{1_k}, b_k} \cong 2\mathbf{b}^T \frac{\partial \mathbf{H}^T}{\partial a_1} \mathbf{Q} \frac{\partial \mathbf{H}}{\partial a_1} \mathbf{b} \Big|_{a_{1_k}, b_k} \quad (26)$$

where the partial derivative of $\mathbf{H}$ was defined in Eq. 21. Utilizing the approximation on the second derivative makes this a Gauss-Newton method. The minimization is obtained by setting the derivative with respect to a_1 equal to zero, which yields the new estimate of a_1:

$$a_{1_{k+1}} = a_{1_k} + \frac{\mathbf{b}^T (\partial \mathbf{H}^T/\partial a_1)\, \mathbf{Q}(\mathbf{y} - \mathbf{H}\mathbf{b})}{\mathbf{b}^T (\partial \mathbf{H}^T/\partial a_1)\, \mathbf{Q}\, (\partial \mathbf{H}/\partial a_1)\, \mathbf{b}} \Big|_{a_{1_k}, b_k}. \quad (27)$$

The Gauss-Newton method, which is known to converge quickly for small residual problems, requires only the initialization of a_1. In this case we can obtain a close "guess" by using one of the existing ad hoc algebraic solutions to this estimation problem, i.e., from the Donnelly or Rohlícek algorithms, or, as was done here, another nonunique solution may be used to initialize a_1 very near the optimal value. Given the quality of the initialization, more robust solutions to the NWLS problem, such as the Levenburg-Marquardt method (Dennis and Schnabel, 1983), have not been necessary. Hence the process is initialized with the following a_1 value, and the iterative process is repeated until a convergence criterion is satisfied (e.g., $\epsilon = 0.000005$):

$$a_{1_0} = \frac{A_2 - A_1}{\omega_1(k_2 B_2 - B_1)}, \quad \left|\frac{a_{1_{k+1}} - a_{1_k}}{a_{1_k}}\right| < \varepsilon. \quad (28)$$

Part II: implementation of the nonlinear weighted least-squares solution

Computer simulations were used to examine the quality of the NWLS solution in relation to previous dual-frequency algorithms (Donnelly, 1994; Rohlícek and Rohlícek, 1993; Rohlícek and Schmid, 1994), as well as to theoretical limits. All simulations were implemented with MATLAB 4.2 (The MathWorks Inc., Natick, MA) and run on a 33 MHz, 68040-based Macintosh Quadra 650 (Apple Computer, Cupertino, CA). The basic simulation model uses the complete description of the noise characteristics, including the EPC-9 amplifier (see Barnett, 1995). The simulation model also allowed for the inclusion of linear phase errors (ϕ_e), as might occur because of small unmodeled or uncompensated capacitances present during calibration or general recording, e.g., if $\phi_{e_1} = \phi_e = -0.1°$ at 400 Hz, then $\phi_{e_2} = (k_2/k_1)\phi_e = -0.2°$ at 800 Hz. These phase errors, which produce cross-talk between the real and imaginary components of the measured admittance at each frequency, generally lead to biased estimates.

To test this algorithm on actual cells (and model circuits), we developed a software-based acquisition, estimation, and display program that was integrated into the patch-clamp experimental workstation. This system was built around an existing graphical/numerical program (IGOR Wavemetrics Inc., Lake Oswego, OR) that allows user-developed 'C'-code modules (Kernighan and Ritchie, 1988; Apple Computer, 1993; Wavemetrics, 1994), called XOPs, to be attached to the main program.

The first XOP module (called "Capacitance") provides a parameter setup window that allows the user to define a range of items, including 1) sample interval; 2) frequency and magnitude of stimuli; 3) mode of recording, i.e., continuous or pulsed; 4) display rate (5–20 Hz); and 5) an option for simultaneous amperometry recording. The choices of pulsed stimuli are 1) repetitive square pulses to the same clamping potential; 2) sequences of square pulses to different potentials; and 3) pulses simulating action potentials of varying waveforms. Because the slow-capacitance compensation circuitry of the patch clamp is used to avoid amplifier saturation during pulsed depolarizations, this segment of code must also account for the equivalent compensation signal. It does so by calculating the corresponding correction vectors that are added back to the measured signal vectors to correctly estimate the cell parameters (see Gillis, 1995, for details). This module also provides *P/N* leak subtraction, performed before the capacitance recording, for all pulsed stimuli.

The second XOP module (called "Cap Display") performs the actual stimulation and sampling via the 16-bit A/D card (ITC-16; Instrutech Corporation (1993), Great Neck, NY), as well as the parameter estimation and display of C_m, R_m, R_a, DC membrane current, leak-subtracted pulsed current, and amperometry signal (if selected). The correlated data are saved and can be reanalyzed at a later time by using the third XOP module (called "Estimation"), which implements the ML and NWLS solutions as well as other dual-frequency and single-frequency methods for comparison purposes.

System calibration

The system was calibrated to account for the effects of the D/A conversion and the various patch-clamp filters, in both the stimulus and signal pathways, on the final sampled current. The calibration data, obtained once and then saved indefinitely, consisted of the magnitude and phase characteristics of the system at the two stimulus frequencies. The

actual calibration procedure consisted of 1) neutralization of any residual capacitance using the fast capacitance compensation circuitry; 2) placement of a 500-kΩ resistor (with low parasitic capacitance) in the head stage of the amplifier; and 3) stimulation of the system with the complete range of stimulus frequencies used by the estimation software. The output current, averaged over several seconds to reduce the noise, is subsequently used to calculated the amplifier magnitude (Γ) and phase (ϕ) characteristics, as well as a new $\mathbf{D}$ matrix with the calibrated column vectors

$$\mathbf{C}_f = V_f\Gamma_f\begin{bmatrix}\cos(\phi_f)\\ \cos\left(\frac{2\pi k_f}{N}+\phi_f\right)\\ \vdots\\ \cos\left(\frac{2\pi k_f}{N}(N-1)+\phi_f\right)\end{bmatrix},$$

$$\mathbf{S}_f = V_f\Gamma_f\begin{bmatrix}\sin(\phi_f)\\ \sin\left(\frac{2\pi k_f}{N}+\phi_f\right)\\ \sin\left(\frac{2\pi k_f}{N}(N-1)+\phi_f\right)\end{bmatrix}. \quad (29)$$

Frequency selection

The choice of stimulation frequency pair clearly affects the performance of the estimator. In the case of single-frequency stimulation, the intuitive selection might be the pole frequency, where the change in the admittance with respect to changes in capacitance is a maximum. However, because the noise increases with frequency similar to $\partial Y/\partial C_m$, the actual optimum single frequency (f_{opt}) can be significantly lower. Gillis presented an expression for capacitance estimate noise (neglecting R_m), in the L-N technique, and a range of acceptable frequencies, f_l to f_h (Gillis, 1995), bounded by the following values:

$$f_{opt} = \frac{1}{2\pi(R_m R_p^3 C_m^4)^{0.25}},\quad f_l = \frac{1}{2\pi\sqrt{R_m R_p C_m}},\quad f_h = \frac{1}{2\pi R_p C_m}. \quad (30)$$

When using two frequencies, there is no simple expression to select an optimum pair, because of the many, often conflicting, variable parameters. Critical factors include the overall voltage excursion allowable before voltage-dependent channels are activated, in which case a frequency ratio of $k = 2$ is superior to $k = 3$ for equal-magnitude stimuli, and the desired estimation rate, which limits the lowest frequency. The following are a few practical guidelines: 1) R_m estimates improve at lower frequencies; 2) R_a estimates improve at higher frequencies; 3) frequencies that lie in the "optimal" range presented in Eq. 30 produce the best C_m estimates; 4) generally, a higher frequency ratio produces improved estimates in R_m and C_m at the cost of larger voltage excursion; and 5) changes in cell parameters that shift the pole of the transfer function to a higher frequency, e.g., decreasing R_a or R_m or C_m, cause a similar shift in the optimum stimulus frequency range. For example, Fig. 4 *a* illustrates that while holding R_a and C_m fixed, lowering R_m results in a minimum CRB that shifts to a higher frequency range (CRB plotted as a function of the lower stimulus frequency for a fixed estimation rate of 100 Hz). Fig. 4 *b* depicts a similar situation, where R_a and R_m are fixed while C_m is varied. In this case, a large value of C_m creates a very limited range of optimal frequency selection because of the relatively narrow bandwidth (f_l = 113 Hz, f_h = 811 Hz, f_{opt} = 303 Hz), where C_m strongly influences the admittance.

Simulation results

Several variations of the NWLS solution (i.e., different weight matrices) were examined to analyze the cost-performance benefits of more complicated, and hence more realistic, models of the inverse covariance matrix. In the first case, the weight matrix was set to the inverse of the covariance matrix, evaluated at the previous estimate, which essentially corresponds to the ML solution based on the reduced data set. Next, by approximating the covariance matrix as the diagonal matrix defined in Eq. 18, we examined the effect of ignoring the full structure of the covariance matrix and simply weighting the data by the SNR at the stimulus frequencies. This approximation allows for a faster algorithm by taking advantage of the diagonal matrix structure in the matrix products contained in the NWLS algorithm. Finally, we examined the matrix $\mathbf{Q} = \mathbf{D}^T\mathbf{D}$, which completely ignores the noise structure (which is equivalent to a white-noise assumption). These three variations were tested and compared with both the CRB for the reduced data and with the CRB obtained from the raw data set.

The data presented in Fig. 5 are representative of a perforated-patch recording of a typical pancreatic islet β-cell or rat adrenal chromaffin cell. In this case, the base parameters were C_m = 5 pF, R_a = 20 MΩ, and R_m = 1000 or 100 MΩ, thus examining both the high and low mem-

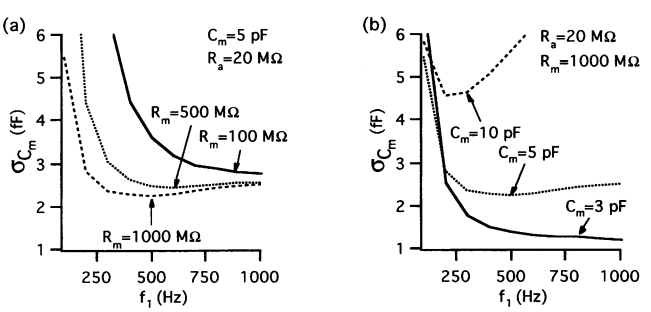

FIGURE 4 Rationale for frequency selection depends on parameter values, allowable voltage excursion, and the value placed on minimizing a particular parameter variance. (*a*) In this unfiltered case, where $V_1 = V_2$ = 10 mV and $f_2 = 2f_1$, decreasing R_m shifts the optimal lower stimulus frequency to a higher range. (*b*) Similarly, for the same stimulus parameters but holding R_m constant, increasing C_m shifts the optimal stimulus pair to a lower range.

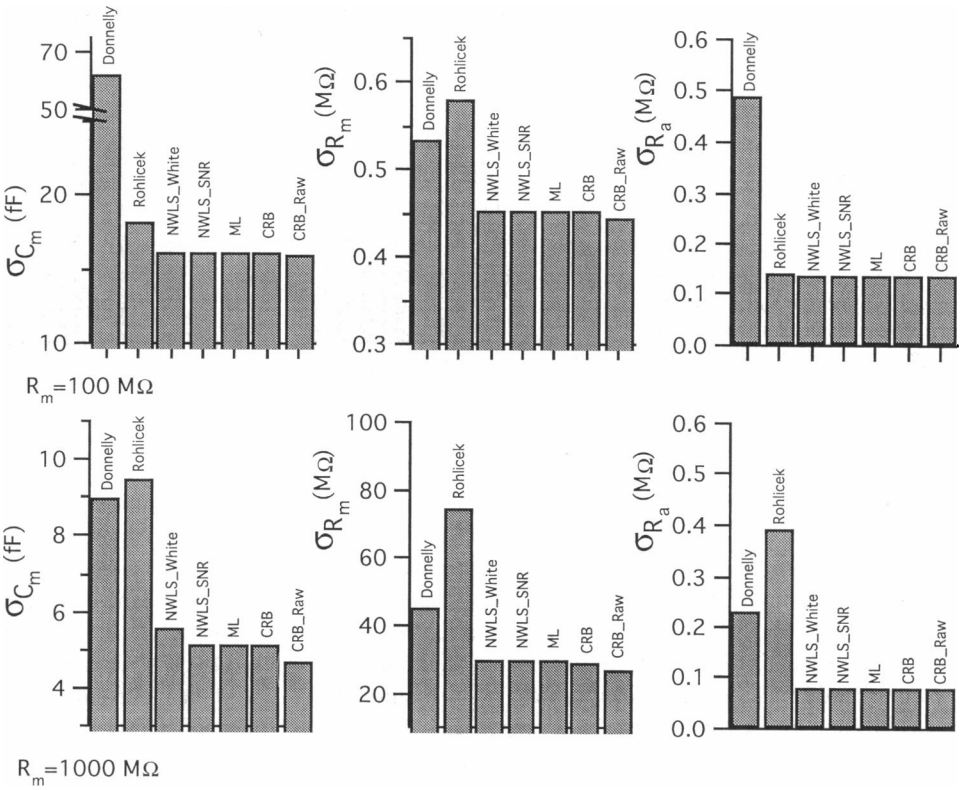

FIGURE 5 Simulation results indicating that the nonlinear weighted least-squares solution, which accounts for the general shape of the noise spectrum (NWLS SNR), reaches the minimum bound for the reduced data set (CRB). In this example, the base parameters were C_m = 5 pF, R_a = 20 MΩ, and R_m = 1000 MΩ (*bottom*) or 100 MΩ (*top*). The other bars correspond to the raw data Cramér-Rao bound (CRB Raw), the approximate maximum-likelihood solution (ML) using the inverse of the reduced data covariance matrix as the weight matrix in the NWLS algorithm, the NWLS solution under a white noise assumption (NWLS White), and the previously published dual-frequency methods (Donnelly or Rohlícek). Note that the estimates are unfiltered (M = 1)

brane resistance cases. A total of five different models were tested and compared to the two theoretical limits. The columns of Fig. 5 represent 1) the Donnelly and 2) Rohlícek algorithms, the NWLS solution with diagonal weight matrices corresponding to 3) the false white-noise model and 4) the SNR approximation, 5) the reduced data ML solution, and finally, 6) the reduced data CRB and 7) the raw data CRB. For each case, the stimulation was V_1 = 10 mV, f_1 = 400 Hz, V_2 = 10 mV, f_2 = 800 Hz. All estimates were calculated using 1024 single sample vectors (M = 1, the unfiltered case), corresponding to the fastest estimation rate. Increasing the M-factor reduces the estimate noise, in terms of standard deviation, by $1/\sqrt{M}$. All parameter estimates were virtually unbiased ($C_{m,bias} < 1$ fF, $R_{a,bias} < 10$ KΩ, $R_{m,bias} < 0.1$ MΩ for R_m = 100 MΩ, $R_{m,bias} < 4$ MΩ for R_m = 1000 MΩ).

Based on simulations, the ML estimate is essentially efficient, i.e., it reaches the CRB. Furthermore, although there exists a clear difference between the full data set CRB and the reduced data CRB, the increase is typically less than 10% (using these basic cell model parameters), which is acceptable, considering the additional computational and system requirements. The NWLS solution using the SNR-based weight matrix is equivalent to the ML solution under both high and low membrane resistance test conditions. In fact, even the solution that ignores the shape of the noise spectrum performs well under both conditions (the quality of the C_m estimate actually improves when the membrane resistance is low because of the fact that as R_m decreases, the noise becomes increasingly white). However, the performance of this approach (i.e., using $\mathbf{Q} = \mathbf{D}^T\mathbf{D}$) does deteriorate when the frequency spread is increased or, in general, whenever the cell parameters are such that the noise spectral density differs greatly between the two stimulus frequencies. All implementations of the NWLS algorithm provided significant improvements when compared to existing dual sinusoidal stimulus methods.

Model circuit results

To verify the software and test the capabilities of the estimation algorithm, a model circuit was used to mimic the cell electrical behavior. Using an EPC-9 model circuit (HEKA), estimates were generated (5.1 MΩ, 500 MΩ, 22 pF) and noise levels were compared to the CRB and to simulations based on the nominal values (see Fig. 6). The stimulus frequencies were 400–800 Hz, both with 10 mV magnitude. The postprocessing estimates for 60 s of data, using 40 sample vectors per estimate, were processed in 3 s for the NWLS method (8 iterations required for convergence) or 94 s for ML (10 iterations). There was no apparent difference between estimates when the slow capacitance compensation was used.

Results from rat adrenal chromaffin cells

A series of experiments on rat adrenal chromaffin cells were performed to assess the performance of the NWLS algorithm under actual experimental conditions. To examine the optimality issue, the noise levels from a range of baseline

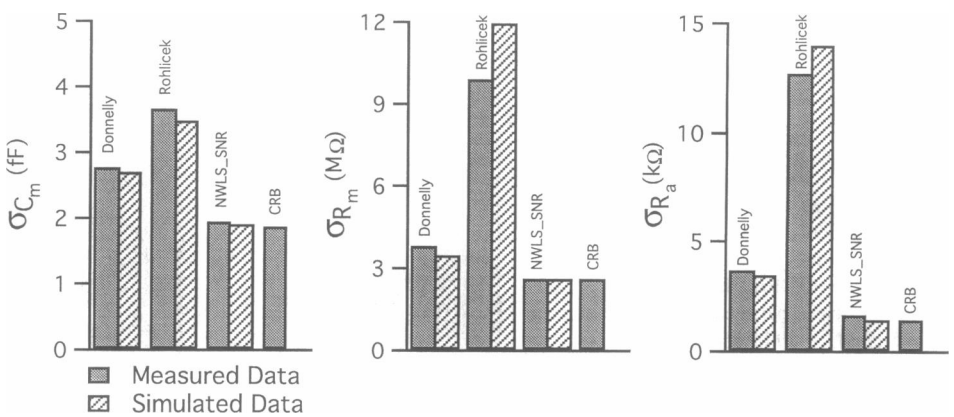

FIGURE 6 Model circuit results confirming computer simulations of dual-frequency estimation algorithms (Donnelly, Rohlícek, NWLS with the signal-to-noise ratio approximation to the covariance matrix, and the reduced-data Cramér-Rao bound). The model circuit consisted of 5.1 MΩ, 500 MΩ, and 22 pF. The stimulus was $V_1 = V_2 = 10$ mV at $f_1 = 400$ Hz, $f_2 = 800$ Hz. ▩, Estimates generated from the measured data; ▨, reults from a simulation based on the nominal values. Estimates were generated using 40 sample vectors per datum.

cell values were compared to the calculated CRB ($n = 10$, 5 pF $< C_m <$ 10 pF, 800 MΩ $< R_m <$ 1400 MΩ, 15 MΩ $< R_a <$ 30 MΩ). Overall, the C_m and R_m estimates were only marginally noisier than predicted (1.4 for C_m and 1.2 for R_m), whereas R_a proved to be nearly 3.4 times the CRB level. The susceptibility of R_a estimates to noise sources beyond our ideal model (e.g., electronics, basal membrane exocytosis and endocytosis, finite seal resistance, etc.) may be partially attributed to the fact that the stimulus frequencies are generally selected to focus on C_m and R_m. Comparison of NWLS estimates to previous dual-frequency methods showed that the uniform improvements predicted via simulation were also found in real cells. The NWLS C_m estimates displayed 42% (or 33%) lower noise than the Rohlícek (or Donnelly) solutions. R_a estimates were typically improved by 20% in both cases, whereas estimates of R_m could not be directly compared, because the other algorithms were susceptible to large biases as the baseline R_m value increased (Donnelly tended to overestimate, whereas Rohlícek underestimated). Whereas all of the dual-frequency methods were unbiased in "ideal" simulation trials, when small linear phase errors (≤0.5°) were included in the model the greater sensitivity to R_m bias found in the Donnelly and Rohlícek algorithms became evident.

As has been noted previously (see Gillis, 1995), dual-frequency methods are generally noisier than single-frequency techniques. Therefore we examined the ability of the NWLS technique to measure the membrane capacitance change associated with the release of one or more secretory granules from rat chromaffin cells. Data presented in Fig. 7 demonstrate the exocytotic response of a rat chromaffin cell to a train of 10 simulated action potentials (APs). These pseudo-APs, which provide only a small amount of Ca^{2+} entry (see current trace), evoke capacitance steps in the range of a few femtofarads (0–6), as might be expected from one or two "typical" chromaffin granules (200–300 nm diameter).

In Fig. 7 the capacitance trace is shown for two filter settings to illustrate the tradeoff between parameter noise reduction and the time response. In the first case, where 50-ms of current samples are used per datum, the measured capacitance noise is approximately $\sigma = 1.8$ fF. However, by increasing the averaging time to 800 ms, the noise is reduced to $\sigma = 0.6$ fF, at the cost of limiting the response time of the algorithm. These experimental numbers correspond well with the theoretical CRB based on the estimated cell parameters and the SNR of this recording ($\sigma = 1.6$ and 0.55, respectively). Because the capacitance measurement noise is Gaussian, we can easily establish a threshold change in capacitance for a particular probability of false alarm (P_{FA}). In this example, using the 800-ms filtered data, the threshold is $\Delta C_m = 1$ fF for the case of $P_{FA} = 0.05$, which means that changes in capacitance greater than 1 fF are relatively unlikely to be the result of recording noise. To

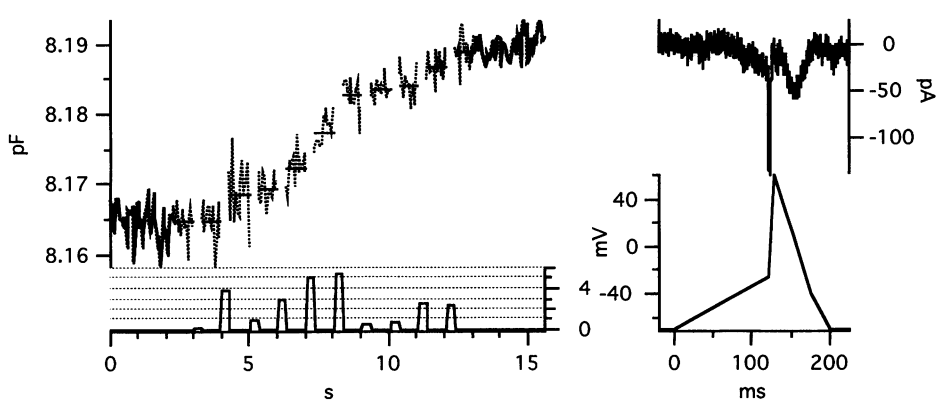

FIGURE 7 Measurements of capacitance steps, evoked from a train of simulated action potentials (AP), from a rat adrenal chromaffin cell (Cs^+-IS, TEA_{50}-ES). (*Left*) Ten repetitive pseudo-AP voltage-clamp pulses, given at 1 Hz, produce capacitance steps that correspond to the fusion of one or two "typical" (2–3 fF) chromaffin granules. (*Right*) The shape and time course of the AP voltage-clamp pulse and the resultant current.

reduce the P_{FA} we must 1) move the threshold to a larger value, 2) increase the filtering time, or 3) increase the SNR by enlarging the stimulus voltages, a maneuver that will eventually be limited by the maximum allowable voltage excursion.

Whereas the P_{FA} can be controlled, to some extent, by altering the recording conditions, the probability of detecting the fusion of one or more granules is a function of the granule size and size distribution. Early measurements of epinephrine-containing vesicles in bovine chromaffin cells indicated that there is a broad distribution of diameter size (Coupland, 1968). A Gaussian fit of Coupland's data results in a density function that is characterized by a mean diameter of 348 nm and a standard deviation of 123 nm. However, to account for the skew of the data, a better fit may be obtained from a general Gamma density function, $f_x(x) = (c^b/\Gamma(b))x^{b-1}e^{-cx}u(x)$, where $b = 7.9$ and $c = 0.9$. This function is subsequently used to form the density function describing the capacitance of a single vesicle, which is proportional to the square of the diameter.

Using this characterization of the capacitance size and the threshold of $\Delta C_m = 1$ fF, the probability of detecting the fusion of a single vesicle in Fig. 7 is $P_D = 0.93$, and the probability of missing a single fusion event is $P_M = 0.07$. The single fusion event, as opposed to multiple granule fusion, is clearly the limiting case. However, the separation of the number of vesicles fused is not possible, with any statistical significance, because of the broad distribution of granule diameters. Finally, there have been other studies characterizing granule size reported in the literature that vastly differ from that reported by Coupland for both rodent (Doupe et al., 1985) and bovine chromaffin cells (Glavinovic et al., 1996). These reports of smaller diameters (~200 nm) will reduce the P_D for a single event but, to reemphasize, they will have no effect on the P_{FA}.

Rat chromaffin cells are known to have small conductance Ca^{2+}-activated K^+ channels (SK) (Park, 1994) that can produce dramatic changes in membrane conductance due to depolarization-induced Ca^{2+} entry. This case is illustrated in Fig. 8, where a train of depolarizations (10 200-ms duration pulses from −70 to +10 mV applied at 1 Hz) induces a large drop in membrane resistance (800 to 100 MΩ) over the course of the pulsing sequence (10 s) that is evident from the development of a large membrane current (I_m). However, while the value of R_m drops, the R_a estimate is relatively unaffected and the C_m estimate indicates a delayed exocytotic response to the Ca^{2+} entry that is supported by a similar time course in the amperometric recording. The integral of the amperometric recording, representing the total amount of secretory products detected by the carbon fiber, is well aligned with the capacitance trace (see Fig. 8 *b*, *middle*). The total number of amperometric events detected (i.e., the number of amperometric spikes) represents approximately 25% of the number of events predicted from the capacitance estimate, which is typical of amperometric recordings (Zhou and Misler, 1995).

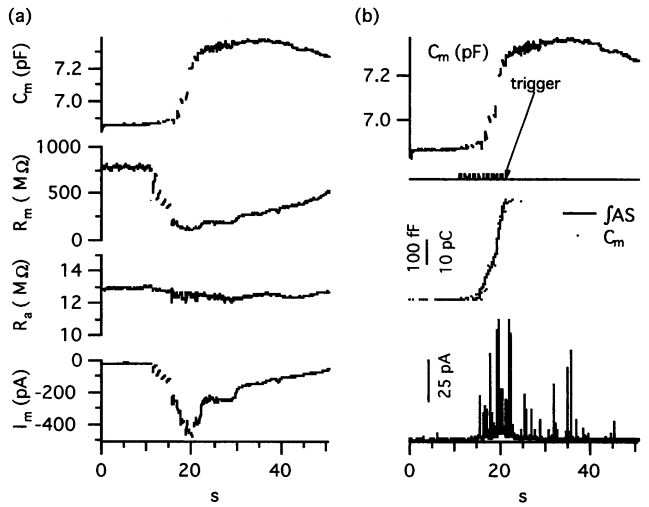

FIGURE 8 Secretion from rat adrenal chromaffin cell measured simultaneously by capacitance estimation and amperometric detection of catecholamines (Cs^+-IS, ES). (*a*) In this case, 10 repetitive voltage-clamp pulses (200 ms to +10 mV) are given at 1 Hz to evoke a large secretory response. Note the development of a large inward current, due to an increasing membrane conductance, does not affect the estimation of R_a or C_m. (*b*) The time course of C_m increments closely matches the time integral of the amperometric current.

Contribution of large conductance changes to capacitance transients

During the examination of capacitance changes induced by single, widely spaced pulses, we observed that when conductance changes were extremely large (increasing to >5 nS), there appeared to be growing cross-talk from the R_m record to the C_m trace and, to a lesser extent, the R_a trace (see Fig. 9). These C_m transients persisted, even after the correction for possible gating charge artifacts (Horrigan and Bookman, 1994), and were present in all of the dual-sinusoidal algorithms examined herein, as well as for the LN method. We considered the possibilities that the C_m transients 1) represented an initial, rapid phase of endocytosis,

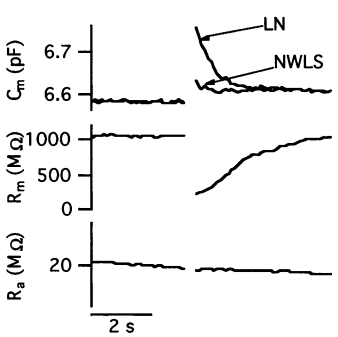

FIGURE 9 Parameter estimates from a rat chromaffin cell (K^+-IS, ES) display cross-talk between the conductance change, due to a large tail conductance, and an early transient rise in the capacitance estimate. Note that the conductance transient produces a larger capacitance transient when the LN algorithm as opposed to the NWLS method is used. The R_m and R_a estimates shown were produced using the NWLS solution.

or 2) were artifacts produced by the large conductance change. To test the second hypothesis, we performed a time-varying circuit analysis of a typical cell model with an exponentially decaying conductance ($g_t = ge^{-\alpha t}u(t)$, where $u(t)$ represents the unit-step function) in parallel with the baseline membrane conductance (see Appendix B). This model was used to simulate the current transients produced by the tail conductance. In the absence of phase errors, the NWLS algorithm is fairly insensitive to these transients. However, when combined with small linear phase errors, the transients can account for the cross-talk between the large conductance change and the C_m trace. In addition, our results show that the transient current alone, without phase errors, is sufficient to account for the large capacitance transients produced by the LN algorithm in cases where the reversal potential shifts, even slightly, because of the large transient conductance.

Using this analysis, we characterized the response of the estimation algorithm due to a range of estimation parameters. The maximum cross-talk between the conductance change and the capacitance trace occurred when the time constant ($\tau = 1/\alpha$) was approximately the same as the period of the fundamental stimulus frequency, e.g., when $f_1 = 400$ Hz and $M = 1$, the peak occurred when $\tau = 3$ ms. As the filtering parameter (M) was increased, the capacitance transient (ΔC_m) decreased and the location of the peak shifted to longer time constants that roughly corresponded to the integration time per estimate (i.e., M/f_1). In addition, for a fixed time constant, increasing M results in R_m estimates that increasingly underestimate the change in membrane resistance (ΔR_m).

In the absence of phase errors, which produce cross-talk between the real and imaginary components of the admittance measurements, estimates produced by the NWLS algorithm were fairly insensitive to conductance changes (see Fig. 10 *a*). When these phase errors are included in the analysis, they tend to produce a plateau level, past the peak transient, that is not highly dependent on the time constant of the conductance. Over small angles ($\pm 1°$), the phase errors produce results that vary linearly with the angle, as might be expected, because the admittance projections are nearly linear for small ϕ_e (i.e., $\sin(\phi_e) \approx \phi_e$). If the Nernst potential of the transient conductance (E_t) is the same as the reversal potential (E_r), then the capacitance cross-talk found in the LN method is nearly identical to that produced by the NWLS algorithm (*lower traces*). However, even small changes in E_t can produce large cross-talk because of the fact that the LN method is highly sensitive to errors in reversal potential when the conductance is large. The upper traces of Fig. 10 *a* illustrate two cases of this sensitivity ($E_t - E_r = -1$ and -5 mV) for a large conductance change ($g = 10$ nS). The sensitivity of the LN algorithm to E_t is further illustrated in Fig. 10 *b*. In this case ($C_m = 5$ pF, $R_m = 1000$ MΩ, $R_a = 20$ MΩ, $g = 10$ nS, $\tau = 0.5$ s, $V_{DC} = -70$ mV, $E_r = -65$ mV, $\phi_e = -0.1°$), we find the NWLS results to be relatively insensitive to E_t (*left axis*), whereas the LN method is highly dependent on E_t (note different scale on *right axis*).

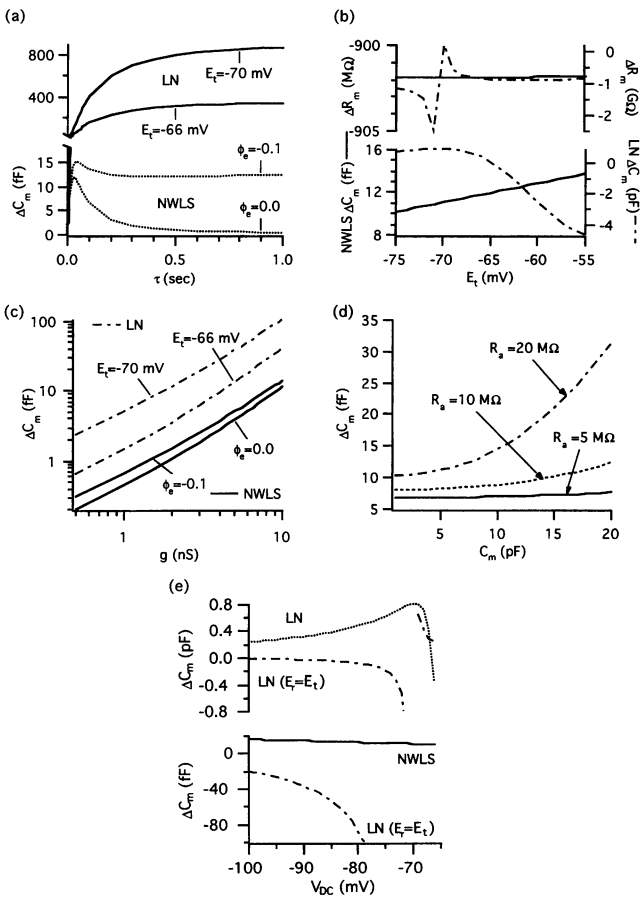

FIGURE 10 Simulations of the cross-talk effects due to a large, exponentially decaying, membrane conductance (see Appendix B). (*a*) In the absence of phase errors the NWLS estimate of capacitance is only marginally affected by a large conductance change ($C_m = 5$ pF, $R_m = 1000$ MΩ, $R_a = 20$ MΩ, $g = 10$ nS, $\tau = 0.5$ s, $V_{DC} = -70$ mV, $E_r = -65$ mV, $M = 40$), with the peak cross-talk transient (ΔC_m) occurring when the time constant is roughly equal to the estimation rate. Addition of a small linear phase error ($\phi_e = -0.1°$) essentially provides a plateau ΔC_m level for the NWLS algorithm (although it increases slightly as a function of τ). In the LN method, small shifts from the reversal potential ($E_r = -65$) due to the potential associated with the new conductance (E_t) result in larger ΔC_m's. (*b*) For the same cell parameters (and $\phi_e = -0.1°$), the NWLS method (*left axis*) provides a close approximation to the change in membrane resistance (ΔR_m) and ΔC_m levels that are only slightly affected by E_t. However, the LN estimates are highly dependent on E_t because of the high conductance (*right axis*). (*c*) Maintaining all other parameters constant, increases in g result in a supralinear increase in ΔC_m (1.5–2.0). (*d*) The NWLS cross-talk effects increase with increasing R_a, holding C_m constant, or with increasing C_m, holding R_a constant. (*e*) For a fixed E_t (−70 mV), the NWLS algorithm is fairly insensitive to the holding potential (V_{DC}), whereas the LN method improves as V_{DC} moves away from E_t. Use of transient reversal potential in the LN algorithm (set $E_r = E_t$) further improves the capacitance estimate.

The variation in cross-talk as a function of the magnitude of the transient conductance is depicted in Fig. 10 *c*. Fixing all other parameters, the relationship between capacitance transient size and g is supralinear, generally with a power of 1.5–2.0. This behavior coincides with the analysis of Ap-

pendix B, which describes the time-varying membrane potential in terms of an alternating power series in g, where the first few coefficients are the most significant. In Fig. 10 *c* we illustrate that this relationship occurs both with and without phase errors (for NWLS) and for different changes in reversal potential (for LN). For the case of varying cell parameters, Fig. 10 *d* shows that the NWLS method produces a larger ΔC_m, for a fixed cell size, as the access resistance increases. Similarly, for a fixed R_a, the C_m transient increases as the baseline C_m increases. Finally, Fig. 10 *e* illustrates the relationship between cross-talk and holding potential (V_{DC}). Whereas the overall performance of the NWLS algorithm is relatively unaffected by V_{DC}, the LN method improves as the holding potential is moved away from the reversal potential of the transient conductance. However, the cross-talk seen with the LN method is still significantly larger than the NWLS estimates, unless the algorithm uses the transient reversal potential (E_t) in place of the reversal potential before the opening of the transient conductance (E_r). This technique produces much improved capacitance estimates, as long as E_t does not approach V_{DC}, although the cross-talk is still larger than the NWLS method because of 1) the time-varying nature of the true reversal potential and 2) the fact that an exponentially decaying current has a DC component that is larger than the components measured at the frequencies of the AC-based stimulus. In addition, the LN approach results in biased estimates of R_m as the conductance closes down and reversal potential returns to E_r.

The time course of the cross-talk transients, for a typical perforated-patch recording from a rat adrenal chromaffin cell (C_m = 5 pF, R_m = 1000 MΩ, R_a = 20 MΩ), is illustrated in Fig. 11 *a* for varying g (2, 5, and 10 nS) and in Fig. 11 b for varying τ (0.1, 0.5, and 1 s). Because the closure of SK channels in rat adrenal chromaffin cells produces tail currents with long half-decay times (τ = ~0.5–1 s for 200-ms depolarizations; Park, 1994), these simulations reflect parameter values that may be encountered experimentally. To substantiate the model of transient cross-talk, we compared experimental data from rat chromaffin cells that displayed large conductance transients and ΔC_m's (recall Fig. 9) with simulated data. Using typical SK channel parameters for a rat chromaffin cell (Park, 1994), the model's transient conductance value was varied such that the estimated size and time course of the R_m recording were well matched by the estimation algorithm. In Fig. 11 *c*, the large but slowly decaying membrane resistance was fit using g = 4.5 nS and τ = 0.8 s. Inclusion of a small phase error (ϕ_e = −0.1°) was required to properly fit the C_m transient produced by the NWLS algorithm.

Using the same baseline parameters, the predicted errors in the capacitance estimate produced by the LN algorithm are also well modeled (see Fig. 11 *d*). In addition, the large resistance transient apparent in the LN estimate of R_m is also replicated (V_{DC} = −70 mV, E_r = −64 mV, E_t = −71 mV). Although this example represents a worst-case scenario of application of the LN method, because E_t is near V_{DC}, it

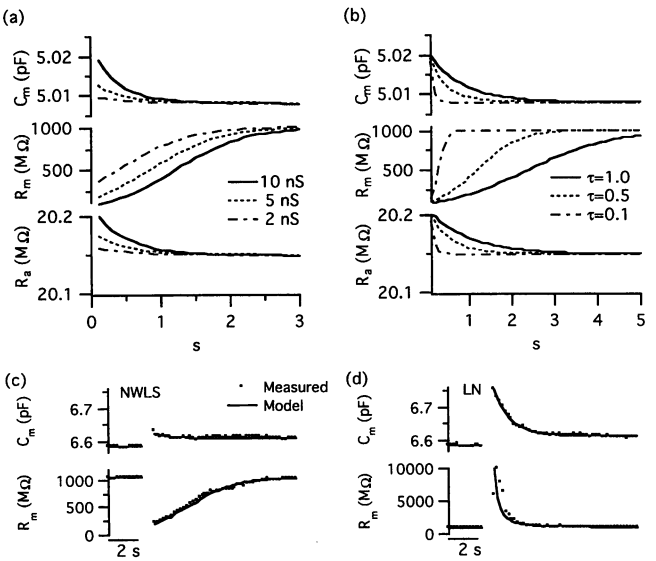

FIGURE 11 (*a*) The time course of NWLS estimates (ϕ_e = −0.1°), as simulated with one time constant (τ = 0.5 s) but for varying levels of g, indicates the increasing effect on both ΔC_m and ΔR_a. (*b*) Similar graph depicting the effect of varying τ while maintaining a constant g (g = 10 nS). The initial ΔC_m's are essentially the same size, because these time constants are in the plateau area shown in Fig. 10 *a*. To verify the computer model, the C_m and R_m estimates shown in Fig. 9 (from a rat adrenal chromaffin cell) are modeled by the transient membrane conductance simulation. (*c*) The NWLS R_m estimate is fit using g = 4.5 nS, τ = 0.8 s. The C_m cross-talk requires the inclusion of a small linear phase error (ϕ_e = −0.1°) to account for the small transient. (*d*) Based on the same model parameters and the appropriate DC potentials (V_{DC} = −70 mV, E_r = −64 mV, E_t = −71 mV), simulation of the LN results agree with the measured data. In this case, the C_m transient is substantially larger and the R_m trace actually indicates a resistance increase rather than a conductance increase.

demonstrates the validity of the transient analysis outlined in Appendix B and thus supports the simulations presented in Fig. 10. Overall, the LN algorithm and the Donnelly method uniformly displayed larger susceptibility to this type of parameter cross-talk than the NWLS method. Whereas the cause of the larger transients in the LN method is due to the shifting reversal potential, the susceptibility of the Donnelly algorithm to cross-talk is not clear, although it does coincide with the fact that the Donnelly estimates become noisier as the conductance increases. Transients in the Rohlícek solution were generally of the same order as in the NWLS method.

DISCUSSION

In a variety of cells, including excitable endocrine cells, neurons, and mast cells, measurements of cell membrane capacitance have been extensively utilized to assay the secretory process by linking changes in membrane surface area, and hence capacitance, to the exocytosis and endocytosis of secretory granules (Fernandez et al., 1984; Augustine and Neher, 1992; Heidelberger et al., 1994; Barnett and Misler, 1995a). Of the currently available techniques, single

sinusoidal-based methods are the most common. However, these techniques are based on assumptions, such as large R_m and/or known E_{rev}, that may not pertain in experimental circumstances in which membrane resistance and capacitance are changing simultaneously. To overcome this problem, Rohlícek (Rohlícek and Rohlícek, 1993; Rohlícek and Schmid, 1994) and Donnelly (1994) proposed the use of a dual-frequency stimulus that provides for an overdetermined system of equations. However, their solutions were not based on an optimal approach to fitting the cell model to the data. In this paper we have examined an optimized, nonlinear weighted least-squares solution that minimizes the variance of the estimates.

In developing an optimized method for estimating the cell parameters, we began by approaching the problem from a classical statistical framework. First we presented a statistical model of the raw current samples that are obtained from the patch-clamp amplifier. In the whole-cell mode of recording, and its perforated patch variant, the primary current noise originates from the membrane resistance and the access resistance of the pipette-cell interface. The noise spectrum of the cell, which is frequency dependent because of the membrane capacitance, is ultimately shaped by the filters in the signal pathway of the patch-clamp amplifier. Hence the covariance matrix of the data is a function of the circuit parameters and the characteristics of the specific patch-clamp amplifier. Although there are advantages to using the complete raw data set, the computer costs in terms of storage, memory, and processor requirements are currently prohibitive. Therefore, we examined a reduced data set, obtained from a dual-frequency digital lock-in detector, consisting of measurements of the complex admittance function at the two stimulus frequencies. Using these reduced data, we compared the parameter variance predicted by the NWLS solution to the theoretical lower bound for variance of unbiased parameter estimates (CRB). By using a weight matrix that is based on the statistical description of the reduced data ($\mathbf{Q} = \mathbf{R}_y^{-1}$), the algorithm produces nearly efficient estimates, i.e., the estimates essentially reach the CRB of the reduced data. Similar results are obtained by using a diagonal weight matrix, based on the SNR at the stimulus frequencies, that compensates for frequency-dependent noise and allows for different stimulus magnitudes.

We have shown that the optimal properties of a complete ML solution, based on the reduced data, can be obtained from a nonlinear weighted least-squares solution to the overdetermined system of equations. This NWLS method, which does not require an exhaustive description of the amplifier, produces results that closely approach the CRB based on the reduced data. However, the CRB established by the complete raw data set was typically about 10% lower. This indicates that reducing the data sacrifices much of the information contained in the noise covariance of the raw current samples. The efficiency of the NWLS estimator can be proved in an asymptotic sense (Gallant, 1987) if we ignore the insignificant contribution of the parameter-dependent noise in the reduced data.

The implementation of the NWLS solution was based on an iterative Gauss-Newton approach that takes advantage of an ad hoc solution to the estimation problem to initialize the algorithm very near the optimal solution. Hence failure to converge is more likely to result from cases in which the three-parameter model is insufficient, thus indicating a problem more severe than algorithm convergence. If this is of concern, implementation of the full Newton method is only a minor extension of the approach presented here. The NWLS algorithm was tested using computer simulations, model circuits, and rat adrenal chromaffin cells. Although capacitance recordings from actual cells were slightly (1.4) noisier than predicted, the efficiency of the model circuit data suggests 1) that the excess noise is due to unmodeled sources, e.g., basal membrane cycling of vesicles; and 2) that the software lock-in is performing satisfactorily, i.e., the excess noise found in the real cells is not due to the use of a software, as opposed to a hardware, lock-in amplifier.

The transient analysis developed here details the conditions under which rapidly developing conductance changes are reflected in the other parameter estimates. This is of particular concern in cells that display prolonged tail currents after extended depolarization, e.g., Ca^{2+}-activated K^+ currents in chromaffin cells (Park, 1994) and Ca^{2+}-activated chloride currents in pituitary cells (Korn and Horn, 1989). These large conductance changes can produce transient changes in capacitance that appear similar to a rapid phase of endocytosis, with the peak cross-talk occurring when the time constant of the exponentially decaying conductance is nearly equal to the base period of the stimulus. This result is similar to the findings of Debus et al. (1995), which showed that the cross-talk due to finite gating kinetics was at a maximum when the rate constant was close to the angular frequency of the sine wave.

Accurate measurements of membrane conductance immediately after a depolarizing pulse allows one to more readily detect the potential for parameter cross-talk and, hence, reduce the risk of misinterpreting the capacitance transients. However, single-frequency methods either "group" the conductance measurements into one channel of the phase-sensitive detector (Neher and Marty, 1982) or are prone to R_m bias because of the unknown E_{rev} (Lindau and Neher, 1988). In the former method, cross-talk generated by a large linear conductance change is relatively small when the phase setting is correct. However, the errors become significantly larger when the phase is misadjusted, which is a condition that may be difficult to avoid (Debus et al., 1995). The NWLS approach is still susceptible to the transient cross-talk produced by a time-varying model, although in many cases the primary source of the cross-talk is actually due to the existence of small phase errors. Although these phase errors are inherent under practical experimental conditions, they can be minimized by careful calibration and capacitance compensation. Even with these phase errors, the NWLS method is much less susceptible to cross-talk than the LN method when the reversal potential shifts from the assumed value because of a large, transient change

in conductance. Under these conditions, the LN method can also produce large errors in the estimate of R_m (especially as E_t approaches V_{DC}), whereas the NWLS method provides a reasonably valid measurement of R_m immediately after conductance change.

One of the primary advantages of using a dual-frequency approach for calculating cell parameters is the ability of these algorithms to generate valid estimates when R_m is low and/or changing during the course of an experiment. Under these conditions, the single sinusoidal based methods generally deteriorate. Although the LN method can be applied to many situations by providing the algorithm with the postulated (or measured) value of the transient reversal potential (E_t), this approach creates C_m estimates that are highly dependent on the E_{rev} chosen. In addition, the use of E_t in the LN algorithm will produce biased R_m estimates as the true reversal potential returns from E_t to the baseline reversal potential (E_r), and furthermore, this solution still fails to account for cases in which E_t shifts toward the holding potential (V_{DC}). This type of researcher-dependent input can be eliminated by using a dual sinusoidal based method to generate on-line, real-time, valid estimates of all three model parameters. Finally, if experimental protocol results in a continuously changing reversal potential, such as the application of a secretogogue that induces the insertion of channels (e.g., α-latrotoxin from the black widow spider; Barnett et al., 1996), then a dual-frequency method is required for estimating the true time course of exocytosis.

The drawback of the dual-frequency method is that the signal is no longer concentrated at one frequency, which generally results in larger parameter variances when the overall stimulus magnitude is held constant. Although this is a function of the frequency and magnitude of each stimulus chosen as well as the noise spectrum, we would roughly expect a single 10-mV signal to produce parameter estimates that are characterized by standard deviations that are $1/\sqrt{2}$ lower than the case of two 5-mV signals. However, as demonstrated here, the NWLS method was able to detect small capacitance steps (>1 fF), such as might be expected from the fusion of a one or more chromaffin granules with the plasma membrane of an adrenal medullary cell. The data shown in Fig. 7 combined moderate stimulus levels ($v_1 = v_2 = 10$ mV) with an 800-ms filter to reduce the probability of false alarm (P_{FA}). To reduce the filtering while maintaining a low P_{FA}, we can utilize more intelligent schemes of selecting the magnitudes and phases of a multifrequency input stimulus such that the waveform provides more energy at each frequency while limiting or shaping the overall voltage excursion. For example, if it is critical to limit the positive voltage excursion, then an appropriate stimulus waveform can be generated using equal magnitude signals, a frequency factor of 2, and a phase shift of 180° on the higher frequency term ($v_1 = v_2, f_2 = 2f_1, \phi_1 = 0°, \phi_2 = 180°$). This waveform exhibits a positive excursion only slightly greater than v_1 but a negative excursion equal to $2v_1$.

In conclusion, our simulations and model circuit results demonstrate the advantages of the NWLS solution, namely, that with appropriately selected weighting factors the NWLS produces efficient parameter estimates. Although this paper discusses a dual-frequency stimulus, extension of the method to include additional stimuli is relatively straightforward. These additional stimuli may be selected, perhaps, such that the voltage excursion is held constant or even reduced. Experiments show that the NWLS algorithm is capable of estimating changes in capacitance while membrane conductance changes by nearly an order of magnitude. This method appears to be less sensitive to the parameter cross-talk induced by large conductance changes than single sinusoidal techniques. The improvements in parameter noise levels (33–42%) offer an advantage over other dual-frequency approaches in a system that is implemented entirely in software and is not amplifier-dependent.

APPENDIX A

The elements of the $\mathbf{R}_y$ matrix, expressed previously as the matrix product $\mathbf{R}_y = (\mathbf{D}^T\mathbf{D})^{-1}\mathbf{D}^T\mathbf{R}\mathbf{D}(\mathbf{D}^T\mathbf{D})^{-1}$, can also be written directly as a summation, so that the relationship to the discrete Fourier transform (DFT) is evident. The individual diagonal elements are given as the sum of two components:

$$\mathbf{R}_{y_{11}} = E\{A_1A_1\} = \alpha_1 + \beta_1 \quad \mathbf{R}_{y_{22}} = E\{B_1B_1\} = \alpha_1 - \beta_1$$
$$\mathbf{R}_{y_{33}} = E\{A_2A_2\} = \alpha_2 + \beta_2 \quad \mathbf{R}_{y_{44}} = E\{B_2B_2\} = \alpha_2 - \beta_2, \tag{A1}$$

where the α and β terms are

$$\alpha_j = \frac{1}{2}\sum_{m=-(N-1)}^{N-1} r(m)\cos\left(\frac{2\pi k_j}{N}m\right)(N - |m|)$$
$$\beta_j = \sum_{m=0}^{N-1} r(m)\frac{-\sin((4\pi k_j/N)\,m)}{1 - \cos((2\pi k_j/N)m)}\sin\left(\frac{2\pi k_j}{N}m\right). \tag{A2}$$

The α term is now recognizable as one-half of the DFT of $r(m)$, the samples of the raw data autocorrelation, times a triangular (or Bartlett) window. In

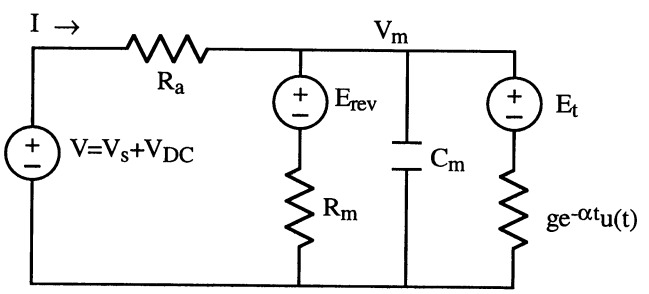

FIGURE 12 Standard cell circuit model, characterized by R_a, R_m, and C_m, is expanded to include an additional tail conductance, $ge^{-\alpha}u(t)$, in parallel with the membrane capacitance and resistance. The voltage sources define the sinusoidal stimulus V_s, the holding potential V_{DC}, the cell reversal potential E_{rev}, and the reversal potential of the transient conductance E_t. The membrane potential, V_m, is at the node separating the access resistance from the membrane circuit elements; the patch-clamp current is labeled as I.

contrast, the β term consists of $r(m)$ times a "sin window," so that it has little effect when $r(m)$ is concentrated near the origin. Hence the α component of the variance is equal to the smoothed power spectrum at that particular frequency, whereas the β component is zero when the noise process is perfectly white, i.e., $r(m) = 0$ for $m \neq 0$.

The off-diagonal elements of $\mathbf{R}_y$, which are much more complicated, also contain a "sin window" effect, as shown below:

$$\mathbf{R}_{y_{12}} = \mathbf{R}_{y_{21}} = E\{A_1B_1\} = \gamma_1 \qquad \mathbf{R}_{y_{34}} = \mathbf{R}_{y_{43}} = E\{A_2B_2\} = \gamma_2$$

$$\mathbf{R}_{y_{14}} = \mathbf{R}_{y_{41}} = E\{A_1B_2\} = \gamma_2 \qquad \mathbf{R}_{y_{32}} = \mathbf{R}_{y_{23}} = E\{A_2B_1\} = \gamma_1$$

$$\gamma_j = -\sum_{m=0}^{N-1} r(m)\sin\left(\frac{2\pi k_j}{N} m\right) \tag{A3}$$

$$\mathbf{R}_{y_{13}} = \mathbf{R}_{y_{31}} = E\{A_1A_2\} = \kappa + \lambda$$

$$\mathbf{R}_{y_{42}} = \mathbf{R}_{y_{24}} = E\{B_1B_2\} = \kappa - \lambda$$

$$\kappa = \frac{1}{2}\sum_{m=0}^{N-1} r(m)$$

$$\cdot\left(\frac{\sin((2\pi k_2/N)\, m) - \sin((2\pi k_1/N)\, m)\sin((2\pi/N)(k_1 - k_2))}{1 - \cos((2\pi/N)(k_1 - k_2))}\right)$$

$$\lambda = \frac{1}{2}\sum_{m=0}^{N-1} r(m)$$

$$\cdot\left(\frac{-\sin((2\pi k_2/N)\, m) - \sin((2\pi k_1/N)\, m)\sin((2\pi/N)(k_1 + k_2))}{1 - \cos((2\pi/N)(k_1 + k_2))}\right).$$

APPENDIX B

Here we examine the effect of a transient membrane conductance change, such as that underlying a slowly decaying tail current after a depolarization, on the estimate of C_m. To accomplish this, we expand the standard three-parameter cell model to include an exponentially decaying conductance, $ge^{-\alpha t}u(t)$, in parallel with C_m and R_m, as shown in Fig. 12. A solution to this time-varying problem will allow us to determine the measured current transients that are used by the capacitance estimation algorithms. Then, by using measurements of tail current size and decay time, we may compare our model with experimental results.

The initial analysis will isolate the sinusoidal stimulus V_s, leaving the contributions of the DC sources, i.e., V_{DC}, E_{rev}, E_t, to be added in later using superposition. Hence we begin by applying Laplace transform techniques to solve for the membrane voltage in the s-domain:

$$V_m(s) = \frac{I_s(s) - gV_m(s + \alpha)}{G_p + sC_m}, \tag{B1}$$

where the current source $I_s(s) = V_s(s)/R_a$ is obtained from a source transformation of the stimulus voltage, and G_p is the conductance associated with the parallel combination of R_a and R_m. In an approach similar to that of Belmont and Matthews (1995) to determine the generalized frequency response, we note that Eq. B1 represents a recurrence relationship, so that we may write

$$V_m(s + \alpha) = \frac{I_s(s + \alpha) - gV_m(s + 2\alpha)}{G_p + \alpha C_m + sC_m}. \tag{B2}$$

By substituting this expression for $V_m(s + \alpha)$ back into Eq. B1 and subsequently repeating the process, we obtain the following series:

$$V_m(s) = \frac{I_s(s)}{G_p + sC_m} + \sum_{n=1}^{N} \frac{(-1)^n g^n I_s(s + n\alpha)}{\prod_{m=0}^{n}(G_p + m\alpha C_m + sC_m)} + \frac{(-1)^{N+1} g^{N+1} V_m(s + (N+1)\alpha)}{\prod_{m=0}^{N+1}(G_p + m\alpha C_m + sC_m)}. \tag{B3}$$

As N goes to infinity, the last term will tend toward zero, so that we may ignore its influence and merely retain the first $I_s(s)$ term, which reflects the membrane voltage without any transient conductance change, and the summation of $I_s(s + n\alpha)$ terms, all of which are s-domain shifted versions of the known stimulus function. A valid expression for $V_m(s)$ can be obtained as long as the summation converges.

We now define the stimulus as $V_0\cos(\omega t)$, which leads to the current source $I_0\cos(\omega t)$ (note that $I_0 = V_0/R_a$), and apply inverse Laplace techniques to obtain the time-domain expression for the membrane voltage. The result for the first term ($n = 0$) and each term of the summation can be written as

$$\frac{I_0(-1)^n g^n (s + n\alpha)}{\prod_{m=0}^{n}(G_p + m\alpha C_m + sC_m)((s + n\alpha)^2 + \omega^2)} = \frac{2\mathrm{Re}\{A\}(s + n\alpha)}{((s + n\alpha)^2 + \omega^2)} + \frac{2\mathrm{Im}\{A\}\omega}{((s + n\alpha)^2 + \omega^2)} + \sum_{m=0}^{n} \frac{B_{nm}}{s + ((G_p/C_m) + m\alpha)}, \tag{B4}$$

where

$$A_n = \frac{I_0(-1)^n g^n}{2\prod_{m=0}^{n}(G_p + (m - n)\alpha C_m - j\omega C_m)},$$

and

$$B_{nm} = \frac{-I_0(-1)^n (g/C_m)^n (G_p + (m - n)\alpha C_m)}{(\prod_{k=0, k\neq m}^{n}((k - m)\alpha))((G_p + (m - n)\alpha C_m)^2 + (\omega C_m)^2)}.$$

The expression for the s-domain membrane voltage can then be written:

$$V_m(s) = \sum_{n=0}^{N}\left(\frac{2\mathrm{Re}\{A_n\}(s + n\alpha)}{(s + n\alpha)^2 + \omega^2} + \frac{2\mathrm{Im}\{A_n\}\omega}{(s + n\alpha)^2 + \omega^2} + \sum_{m=0}^{n} \frac{B_{nm}}{s + ((G_p/C_m) + m\alpha)}\right). \tag{B5}$$

The inverse of the first two terms leads to damped (for $n > 0$) cosine and sine terms, and the last term results in exponential terms with time constants equal to

$$\tau_m = \frac{R_pC_m}{1 + m\alpha R_pC_m} \leq \tau_0. \tag{B6}$$

These purely exponential terms have a very rapid decay time for typical cells ($\tau_0 = R_pC_m = 0.1$ ms for $R_a = 20$ MΩ, $R_m = 1$ GΩ, $C_m = 5$ pF) compared to the period of the stimulus sinusoid (2.5 ms for $f = 400$ Hz), so that their effect is minimal and can essentially be ignored, if after a

depolarizing pulse the first cycle of the sinusoid is not used by the estimation algorithm.

It can be shown via a simple ratio test that the A_n series converges, and in fact, for typical cell parameters this occurred by $N = 5$ (although we usually truncated the sum at $N = 10$). Although the series in B_n also converges, because these rapidly decaying terms have no real effect on the membrane voltage after a fraction of a sinusoidal period, we will not evaluate them directly. Furthermore, because the membrane voltage cannot change instantaneously, the sum of the A_n and B_n terms must equal zero.

For completeness we must also include the DC components that were initially ignored in the circuit model. These sources include the DC holding potential (V_{DC}), the membrane reversal potential (E_{rev}), and the potential source associated with the transient conductance (E_t). By following an identical analysis approach, accounting for initial conditions on the capacitor, and ignoring the insignificant rapid decay terms, the following additional components can be added to the previous expression for $V_m(s)$ of Eq. B5:

$$\frac{C}{s} + \sum_{n=1}^{N} \frac{D_n}{s + n\alpha},$$

where

$$C = \frac{V_{DC}R_m + E_rR_a}{R_T}, \tag{B7}$$

and

$$D_n = \frac{(-1)^n g^n((V_{DC}/R_a) + (E_r/R_m) - (E_t/R_p))}{\prod_{m=0}^{n}(G_p + (m-n)\alpha C_m)}.$$

Therefore, we can now write the time-domain membrane voltage as

$$v_m(t) \cong 2\mathrm{Re}\{A_0\}\cos(\omega t) + 2\mathrm{Im}\{A_0\}\sin(\omega t) + C + \sum_{n=1}^{N} e^{-n\alpha t}(2\mathrm{Re}\{A_n\}\cos(\omega t) + 2\mathrm{Im}\{A_n\}\sin(\omega t) + D_n), \tag{B8}$$

which can be used in the expression for the patch-clamp current:

$$i(t) = \frac{v_s(t) - v_m(t)}{R_a}. \tag{B9}$$

The lock-in amplifier uses this current to determine the in-phase and quadrature components that are used in the estimation algorithms (the DC component can also be calculated for use in the LN algorithm). Equivalently, because the integrals performed by the lock-in involve only exponential and trigonometric functions, we can solve these analytically to determine the "predicted" effects of the transient conductance on the lock-in outputs. The lock-in outputs, as calculated from the time-varying model, can be used in the estimation algorithm to compare predicted capacitance transients to measured data.

We thank Drs. Kevin Gillis and Daniel Fuhrmann for their encouragement and stimulating discussions at the onset of this work and the laboratory of Dr. Chris Lingle for advice and assistance with the preparation of chromaffin cells.

This work was supported by grants from the National Institutes of Health (DK37380) and the Research Foundation of the Barnes-Jewish Hospital of St. Louis. DWB was also supported by a St. Louis University Faculty Research Award.

REFERENCES

Apple Computer, Inc. 1993. Macintosh Programmer's Workshop. Developer Technical Publications, Cupertino, CA.

Augustine, G. J., and E. Neher. 1992. Calcium requirements for secretion in bovine chromaffin cells. *J. Physiol. (Lond.).* 450:247–271.

Barnett, D. W. 1995. Stimulus secretion coupling in pancreatic islet β-cells: studies using membrane capacitance as an assay of exocytosis. D.Sc. dissertation. Washington University, St. Louis.

Barnett, D. W., J. Liu, and S. Misler. 1996. Single-cell measurements of quantal secretion induced by α-latrotoxin from rat adrenal chromaffin cells: dependence on extracellular Ca^{2+}. *Pflügers Arch.* 432:1039–1046.

Barnett, D. W., and S. Misler. 1995a. Coupling of exocytosis to depolarization in rat pancreatic islet β-cells: effects of Ca^{2+}-, Sr^{2+}-, and Ba^{2+}-containing extracellular solutions. *Pflügers Arch.* 430:593–595.

Barnett, D. W., and S. Misler. 1995b. Dual frequency estimation of membrane capacitance and resistance: application of non-linear estimation. *Biophys. J.* 68:A116.

Barnett, D. W., D. M. Pressel, and S. Misler. 1995. Voltage dependent Na^+ and Ca^{2+} currents in human pancreatic β-cells: evidence for roles in the generation of action potentials and insulin secretion. *Pflügers Arch.* 431:272–282.

Belmont, M. R., and J. J. Matthews. 1995. Generalised frequency response as applied to circuits with time varying elements. *IEE Proc. Circuits Devices Syst.* 142:217–222.

Clausen, C., and J. M. Fernandez. 1981. A low-cost method for rapid transfer function measurements with direct application to biological impedance analysis. *Pflügers Arch.* 390:290–295.

Coupland, R. E. 1968. Determining sizes and distribution of sizes of spherical bodies such as chromaffin granules in tissue sections. *Nature.* 217:384–388.

Debus, K., J. Hartmann, G. Kilac, and M. Lindau. 1995. Influence of conductance changes on patch clamp capacitance measurements using a lock-in amplifier and limitations of the phase tracking technique. *Biophys. J.* 69:2808–2822.

Dennis, J. E., and R. B. Schnabel. 1983. Numerical Methods for Unconstrained Optimization and Nonlinear Equations. Prentice Hall, Englewood Cliffs, NJ.

Donnelly, D. F. 1993. Response to cyanide of two types of glomoid cells in mature rat carotid body. *Brain Res.* 630:157–158.

Donnelly, D. F. 1994. A novel method for rapid measurement of membrane resistance, capacitance, and access resistance. *Biophys. J.* 66:873–877.

Doupe, A. J., S. C. Landis, and P. H. Patterson. 1985. Environmental influences in the development of neural crest derivatives: glucocorticoids, growth factors, and chromaffin cell plasticity. *J. Neurosci.* 5:2119–2142.

Fernandez, J. M., M. Lindau, and F. Eckstein. 1987. Intracellular stimulation of mast cells with guanine nucleotides mimic antigenic stimulation. *FEBS Lett.* 216:89–93.

Fernandez, J. M., E. Neher, and B. D. Gomports. 1984. Capacitance measurements reveal stepwise fusion events in degranulating mast cells. *Nature.* 312:453–455.

Fidler, N., and J. M. Fernandez. 1989. Phase tracking: an improved phase detection technique for cell membrane capacitance measurements. *Biophys. J.* 56:1153–1162.

Gallant, A. R. 1987. Nonlinear Statistical Models. Wiley, New York.

Gillis, K. D. 1995. Techniques for membrane capacitance measurements. *In* Single Channel Recording. B. Sakmann and E. Neher, editors. Plenum Press, New York.

Gillis, K. D., and S. Misler. 1992. Single cell assay of exocytosis from pancreatic islet β-cells. *Pflügers Arch.* 420:121–123.

Glavinovic, M. I., M. L. Vitale, and M. Trifaro. 1996. Correlation between vesicular volumes and quantal size in bovine chromaffin cells. *Soc. Neurosci. Abstr.* 22:1241.

Hamill, O. P., A. Marty, E. Neher, B. Sakmann, and F. J. Sigworth. 1981. Improved patch-clamp techniques for high resolution current recording from cells and cell-free membrane patches. *Pflügers Arch.* 391:85–100.

Heidelberger, R., C. Heinemann, E. Neher, and G. Matthews. 1994. Calcium dependence of the rate of exocytosis in a synaptic terminal. *Nature.* 371:513–515.

Heinemann, C., R. H. Chow, E. Neher, and R. S. Zucker. 1994. Kinetics of the secretory response in bovine chromaffin cells following flash photolysis of caged Ca^{2+}. *Biophys. J.* 67:2546–2557.

Horrigan, F. T., and R. J. Bookman. 1994. Release pools and the kinetics of exocytosis in adrenal chromaffin cells. *Neuron.* 13:1119–1129.

Instrutech Corporation. 1993. ITC-16 MAC Computer Interface. Instrutech Corporation, Great Neck, NY.

Joshi, C., and J. M. Fernandez. 1988. Capacitance measurements: an analysis of the phase detector technique used to study exocytosis and endocytosis. *Biophys. J.* 53:885–892.

Kernighan, B. W., and D. M. Ritchie. 1988. The C Programming Language. Prentice Hall, Englewood Cliffs, NJ.

Korn, S. J., and R. Horn. 1989. Influence of sodium-calcium exchange on calcium current rundown and the duration of the calcium-dependent chloride currents in pituitary cells, studied with whole cell and perforated patch recording. *J. Gen. Physiol.* 94:789–812.

Lindau, M., and J. M. Fernandez. 1986. IgE-mediated degranulation of mast cells does not require opening of ion channels. *Nature.* 319: 150–153.

Lindau, M., and E. Neher. 1988. Patch-clamp techniques for time-resolved capacitance measurements in single cells. *Pflügers Arch.* 411:137–146.

Neely, A., and C. J. Lingle. 1992. Two components of calcium-activated potassium current in rat adrenal chromaffin cells. *J. Physiol. (Lond.).* 453:97–131.

Neher, E., and A. Marty. 1982. Discrete changes of cell membrane capacitance observed under conditions of enhanced secretion in bovine adrenal chromaffin cells. *Proc. Natl. Acad. Sci. USA.* 79:6712–6716.

Papoulis, A. 1991. Probability, Random Variables, and Stochastic Processes. McGraw-Hill, New York.

Park, Y. 1994. Ion selectivity and gating of small conductance Ca^{2+}-activated K^+ channels in cultured rat adrenal chromaffin cells. *J. Physiol. (Lond.).* 481.3:555–570.

Penner, R., and E. Neher. 1988. The role of calcium in stimulus-secretion coupling in excitable and non-excitable cells. *J. Exp. Biol.* 139:329–345.

Penner, R., and E. Neher. 1989. Stimulus-secretion coupling in mast cells. *Soc. Gen. Physiol. Ser.* 44:295–310.

Rohlícek, V., and J. Rohlícek. 1993. Measurement of membrane capacitacnce and resistance of single cells using two frequencies. *Physiol. Res.* 42:423–428.

Rohlícek, V., and A. Schmid. 1994. Dual frequency method for synchronous measurement of cell capacitance, membrane conductance and access resistance on single cells. *Pflügers Arch.* 428:30–38.

Scharf, L. L. 1991. Statistical Signal Processing. Addison-Wesley, Reading, PA.

Spanos, J. T., and D. L. Mingor. 1993. Newton algorithm for fitting transfer functions to frequency response measurements. *J. Guidance Control Dyn.* 16:34–39.

van Trees, H. L. 1968. Detection, Estimation and Modulation Theory. John Wiley and Sons, New York.

Wavemetrics, Inc. 1994. IGOR XOP Toolkit. Wavemetrics, Inc., Lake Oswego, OR.

Zhou, Z., and S. Misler. 1995. Action potential-induced quantal secretion of catecholamines from rat adrenal chromaffin cells. *J. Biol. Chem.* 270:3498–3505.

Zhou, Z., and S. Misler. 1996. Amperometric detection of quantal secretion from patch-clamped rat pancreatic β-cells. *J. Biol. Chem.* 271:270–277.

Zierler, K. 1992. Simplified method for setting the phase angle for use in capacitance measurements in studies of exocytosis. *Biophys. J.* 63: 854–856.